Geophysical Journal International

Geophys. J. Int. (2025) **242,** 1–21
Advance Access publication 2025 May 22
Research paper

https://doi.org/10.1093/gji/ggaf188

Frequency-dependent seismic attenuation and velocity dispersion in crystalline rocks: insights from the Grimsel test site

Nicolás D. Barbosa,[1,2] Eduardo A. Besnati,[3] Santiago G. Solazzi,[3] J. Germán Rubino,[4] Emilio Camilión[3] and Klaus Holliger[2]

[1] *SINTEF Industry, 7031 Trondheim, Norway. E-mail: nicolas.barbosa@sintef.no*
[2] *Institute of Earth Sciences, University of Lausanne, CH-1015 Lausanne, Switzerland*
[3] *YPF Tecnología S.A. (Y-TEC), 1923 Berisso, Argentina*
[4] *CONICET, Centro Atómico Bariloche (CNEA), 8400 San Carlos de Bariloche, Argentina*

Accepted 2025 May 13. Received 2025 April 15; in original form 2024 December 19

SUMMARY

Characterizing the hydraulic and geomechanical behaviour of crystalline rocks is of importance for a wide range of geological and engineering applications. Geophysical methods, in general, and seismic techniques, in particular, are extensively used for these purposes due to their cost-effective and non-invasive nature. In this study, we combine legacy seismic observations to analyse the seismic attenuation and velocity characteristics in macroscopically intact regions of the granodiorite hosting the underground Grimsel test site in the central Swiss Alps across a wide frequency range. By focusing on data from the intact rock volumes we aim to assess the importance of viscoelastic effects in the crystalline host rock. Our results show consistent frequency-dependent characteristics of the seismic velocity and attenuation. We illustrate that it is possible to fit a microcrack-related wave-induced fluid flow (WIFF) model to the data over the entire frequency spectrum under examination extending from the Hertz to the Megahertz range. Utilizing complementary pressure-dependent ultrasonic measurements, we infer microcrack properties that validate the key parameters of the proposed WIFF model. These findings deepen our understanding of dispersion and attenuation mechanisms at the microscopic scale in crystalline environments, which is critical for a coherent analysis and integration of data from different seismic techniques as well as for the identification of dispersion and attenuation effects related to macroscale heterogeneities, such as fractures and faults.

Key words: Fracture and flow; Acoustic properties; Body waves; Seismic attenuation; Wave propagation.

1 INTRODUCTION

Crystalline rocks constitute the main host rocks for a wide range of prominent geological and engineering applications. Characterizing the hydraulic and geomechanical behaviour of low-permeability crystalline environments is crucial for ensuring the safety of nuclear waste repositories (e.g. Green & Mair 1983; Majer *et al.* 1990) and the productivity of geothermal reservoirs (e.g. Pandey *et al.* 2018). Furthermore, understanding deformation in surficial crystalline environments is essential for assuring the integrity of critical structures, such as dams, bridges and tunnels (e.g. Zangerl *et al.* 2003; Lüth *et al.* 2008). These applications tend to rely either on the presence of fractures (e.g. fluid flow pathways that ensure circulation in low-permeability geothermal reservoirs) or on their absence (e.g. fracture-induced subsidence may threaten the integrity of structures). As the prevalence of fractures of varying scales, connectivities, transmissivities and compliances is common in crystalline rocks (e.g. Rutqvist & Stephansson 2003), the identification and hydromechanical characterization of these structures is a key factor for the success of these endeavours. In this context, the geophysical and geological characterization of the intact crystalline host rocks is necessary for accurately recovering properties of embedded fractures and faults.

Seismic methods have proven to be powerful characterization and monitoring tools of the heterogeneous subsurface in general and of fractured crystalline rocks in particular. Theoretical and experimental evidence indicates that seismic wave propagation is significantly influenced by various fracture characteristics, including density, size, orientation, aperture and compliance (e.g. Mavko *et al.* 2009). This, in turn, may provide valuable insights into, for example, the fractures that act as the main pathways for fluid flow and pressure relaxation (e.g. Hunziker *et al.* 2020; Barbosa *et al.* 2021). Particularly interesting is the fact that fractured crystalline environments typically exhibit frequency-dependent seismic properties due to both

intrinsic and apparent attenuation and its associated dispersion (e.g. Sarout 2012; Eulenfeld & Wegler 2016). Furthermore, when heterogeneous rocks are fluid-saturated, both mechanisms get significantly modified due to hydromechanical coupling effects (e.g. Pride *et al.* 2004; Müller *et al.* 2010). The so-called wave-induced fluid flow (WIFF) effects arise when the deformation associated with a passing seismic wave creates pressure gradients within the fluid phase of a porous rock. Both at the microscale (i.e. pore scale) and mesoscale (i.e. larger than the pore sizes but smaller than the wavelengths), spatial variations in compressibility promote the development of local gradients in fluid pressure. Neglecting the associated WIFF effects when interpreting seismic data, for example with regard to attenuation, velocity dispersion, anisotropy, scattering, can result not only in inaccurate predictions of the physical rock properties but also in missing the links with other valuable information. Examples of the latter include the relation between amplitude-versus-offset (AVO) data and the degree of fracture connectivity (e.g. Rubino *et al.* 2022), the impact of partial fluid saturation on Rayleigh wave dispersion (e.g. Quiroga *et al.* 2023) and the enhancement of the reflectivity of individual faults (e.g. Sotelo *et al.* 2021). It is important to remark that, as the seismic waves are sensitive to the elasticity contrast between the macroscale fractures and faults and their embedding background, a correct interpretation of WIFF effects relies on the estimation of the seismic properties (e.g. intrinsic attenuation and velocity dispersion) associated with the intact host rock.

In a general scenario, models that account for WIFF effects occurring at either the micro- or mesoscales predict a frequency-dependent seismic response in the upper crust crystalline rocks (e.g. Müller *et al.* 2010). However, incorporating these models into seismic data inversion schemes is as of yet uncommon. The main reason for this is that the most widely used seismic techniques operate within narrow frequency bands: ambient seismic noise monitoring data falls within the sub-hertz range (e.g. Obermann *et al.* 2015); exploration seismic data typically ranges from 10 and 100 Hz (e.g. Crampin & Peacock 2005); high-resolution near-surface seismic data spans the range from hundreds of hertz to a few kilohertz (e.g. Holliger & Bühnemann 1996; Doetsch *et al.* 2020); sonic borehole sources typically operate in the kilohertz range (e.g. Barbosa *et al.* 2019); laboratory-based ultrasonic measurements typically utilize frequencies in the megahertz range (e.g. Batzle *et al.* 2006; Li *et al.* 2018). Describing the characteristics of a frequency-dependent mechanism based on band-limited data poses a challenge. Furthermore, obtaining reliable measurements in the field, particularly with regard to attenuation (e.g. Winkler & Nur 1979; Li & Richwalski 1996; Picotti & Carcione 2006; Gurevich & Pevzner 2015), can be difficult and frequency-dependent effects may be obscured by the inherent uncertainties. In the context of WIFF models, this problem is exacerbated due to the numerous fluid and rock model parameters, the phenomenological similarities in the predicted responses for contrasting models and the typical multiplicity of heterogeneity scales (e.g. Pride *et al.* 2004; Gurevich *et al.* 2009; Gurevich & Pevzner 2015).

As a result of the above-mentioned technical and theoretical challenges, significant gaps still exist between the numerous theoretical models and their experimental validation at the field scale. Over a decade ago, Müller *et al.* (2010) pointed out that, while some of the field observations can be consistently explained with the WIFF mechanism, additional research was necessary to assess the applicability and validity conditions of WIFF models. Many, predominantly laboratory-based, efforts have been made since then to bridge this gap through broad-band experimental studies exploring the dependency of seismic properties on factors such as strain amplitude, frequency, pressure, temperature and fluid saturation. In addition, laboratory studies often involve a combination of two or more techniques (e.g. pulse transmission, resonant bar and forced oscillation techniques) as reviewed by Rørheim (2022). While this relatively well-controlled approach can provide data covering frequencies from hertz to megahertz, caution must be exercised when extrapolating laboratory measurements to field conditions (Adelinet *et al.* 2010). The common reasons being that laboratory measurements may involve idealized, small-scale and/or synthetic rock samples, artificially created cracks, relatively large strains compared to those generated by propagating waves, unrealistic fluid properties (e.g. due to the use of glycerin to shift the frequencies, at which WIFF dominates), unknown saturation states (e.g. residual moisture in the pore space of 'dry' samples), localized measurements of strain (e.g. glued strain gauges measuring local instead of bulk deformation), unrealistic boundary conditions and associated effects (e.g. improper jacketing, dead volume in the fluid drainage system), issues related to misalignments of the samples (e.g. due to rough and/or non-parallel surfaces), transformation of measured parameters (e.g. bulk or Young's moduli) for comparability, among others (e.g. Subramaniyan *et al.* 2014; Ògúnsàmì *et al.* 2021; Rørheim 2022). However, the most significant source of inconsistency between laboratory and field results is arguably the presence of cracks and fractures at various scales, from the pore scale to the wavelength scale, as well as the alteration of original stress conditions when samples are extracted from the subsurface, which can lead to changes in their elastic and hydraulic properties compared to *in-situ* conditions. This complicates the integration of data acquired with dynamic methods having different resolutions and averaging volumes. The work of Sams *et al.* (1997) is the most notable example of data integration, in which vertical seismic profiling (VSP) and sonic log data were combined with ultrasonic measurements from centimetre-scale core samples to determine intrinsic attenuation in a finely layered sequence of limestones, sandstones, siltstones and mudstones. To account for the varying averaging volumes of the techniques considered, the authors computed median values of velocity and attenuation within the same depth interval. While the study provided strong evidence of consistent velocity dispersion and frequency-dependent attenuation across the considered techniques, the presence of heterogeneities made it challenging to determine whether the effects prevailed uniformly for all lithologies.

Therefore, while evidence suggests that frequency-dependent seismic signatures can offer valuable insights into the hydraulic, mechanical and geometrical properties of complex fractured rock masses, the above-mentioned challenges related to data integration, measurement uncertainties and representativeness remain a limiting factor. Efforts to alleviate these problems should focus on meeting conditions that enable a relatively well-controlled quantitative comparison between rock physics models and field measurements. In this sense, the extensive seismic characterization undertaken in the crystalline rocks of the underground Grimsel test site (GTS) in the central Swiss Alps over the last decades presents a unique opportunity to reconcile experimental observations and theoretical predictions. The primary goals of the studies conducted at the GTS were to assess the suitability of crystalline rocks for hosting underground waste repositories and geothermal projects. They focused on characterizing the dominant mechanical and hydraulic features (e.g. shear zones and fractures) while constraining the seismic properties of the intact host rock, the so-called Grimsel granodiorite.

In this work, our primary objective is twofold. First, we want to assess the importance of frequency-dependent effects within macroscopically intact crystalline rocks. To do so, we combine legacy *P*-wave attenuation and velocity measurements that are representative of the macroscopically intact granodioritic host rock across varying survey frequencies. We consider similar stress states and saturation conditions to enable meaningful comparison across the multiple independent data sets. Secondly, we investigate the feasibility of fitting a WIFF model to the frequency-dependent behaviour of the seismic velocity and attenuation in the Grimsel granodiorite. Given that we focus on intact regions of the crystalline rock mass of the GTS, we propose a WIFF mechanism operating at the microscale. In this scenario, energy dissipation is linked to flow occurring within cracks and/or grain boundaries with different shapes, compressibilities or orientations at the microscale.

The work is structured as follows. We first review previously reported measurements (Section 2), which include transmission experiments along tunnels (Majer *et al.* 1990; Holliger & Bühnemann 1996), cross-hole experiments (Doetsch *et al.* 2020), sonic logging (Barbosa *et al.* 2019) and laboratory measurements (Majer *et al.* 1990) on core samples. For each data set, we extract *P*-wave velocities and attenuations whenever available representative of the crystalline host rock as well as the characteristic survey frequency and an estimate of their uncertainties. We complement these legacy data by measuring pressure-dependent ultrasonic data set using samples from the GTS. In Section 3, we analyse the frequency dependence of the attenuation and velocity values in the macroscopically intact Grimsel granodiorite. We then propose a microcrack-related WIFF model to explain the observations over the entire frequency range of observation. Finally, in Section 4, we assess the physical validity of the parameters linked with the proposed WIFF model. In particular, we show that the microcrack properties derived from our pressure-dependent ultrasonic measurements align with those obtained with the fitted WIFF model.

2 SEISMIC ATTENUATION AND VELOCITY MEASUREMENTS REPORTED FOR THE GRIMSEL TEST SITE

In this section, we briefly introduce the GTS as well as the pertinent studies conducted at this site. We sort the latter according to their characteristic survey frequency. Finally, we present newly acquired pressure-dependent ultrasonic data.

2.1 Relevant context

The GTS, which is situated within the crystalline rocks of the so-called Central Aar Massif in the central Swiss Alps, is operated by the Swiss National Cooperative for the Disposal of Radioactive Waste (Nagra). It has an overburden of approximately 480 m and serves as an underground research facility. The tunnels at the GTS (Fig. 1) were drilled with a tunnel-boring machine, resulting in an excavation damage zone of a few meters in width and smooth walls that easily allow measurements on the tunnel walls (Holliger & Bühnemann 1996; Doetsch *et al.* 2020). Various projects of relevance to our study have been conducted at the GTS. Notably, the *In-situ* Stimulation and Circulation (ISC) (e.g. Amann *et al.* 2018) aimed to address key scientific questions related to hydraulic stimulation within enhanced geothermal systems. As part of the ISC project, a comprehensive characterization effort was carried out with the primary objective of creating a 3-D model of the geological structures, rock properties, stress distribution and hydraulic characteristics of the investigated volume. In addition to the main tunnels, two boreholes dedicated for the high-pressure fluid injections (INJ-boreholes) and four boreholes dedicated for geophysical monitoring (GEO-boreholes) were used for geophysical borehole measurements within the framework of the ISC project (Doetsch *et al.* 2020). Specifically, seismic transmission experiments, such as cross-hole tomography, proved to be valuable techniques for identifying fracture zones within crystalline rock formations (Majer *et al.* 1990; Doetsch *et al.* 2020).

The geophysical characterization of hydraulic stimulations at GTS not only enabled time-lapse monitoring of the underlying processes but also allowed to identify valuable links between the hydraulic and mechanical response of fractures. For example, Barbosa *et al.* (2021) showed that the fracture normal compliance Z_N, which quantifies the fracture's mechanical behaviour under stress, correlates with the fracture's hydraulic transmissivity, as obtained from various hydraulic characterization experiments performed within the ISC project (Dutler *et al.* 2019; Brixel *et al.* 2020; Krietsch *et al.* 2020). In this context, Barbosa *et al.* (2019) developed a technique which allowed for the quasi-continuous estimations of fracture compliance along a borehole. Central to the proposed methodology is the computation of fracture-related transmission losses from attenuation estimates, which requires removing the contributions associated with other amplitude loss mechanisms, such as geometrical spreading and intrinsic background attenuation. When applying this methodology to full-waveform sonic (FWS) log data acquired along INJ2 (Fig. 1), the authors found that the host rock intrinsic attenuation, estimated from measurements in intervals of intact granodioritic rock, was rather high as quantified by quality factors Q between 12 and 14.5. Interestingly, these Q-values were consistent with earlier estimates from the GTS (Majer *et al.* 1990; Holliger & Bühnemann 1996) for frequencies that were several orders-of-magnitude lower. However, the underlying cause of this relatively high intrinsic attenuation in the macroscopically intact crystalline host rock remains unexplored. Our objective is to quantitatively assess the consistency of the seismic attenuation and velocity observations across the multiple studies and to propose a plausible physical mechanism to comprehensively explain all available observations.

To this end, we have selected *P*-wave seismic data with the aim of enabling a meaningful comparison across the various data sets that may provide insights into the mechanisms behind the observed seismic properties. These data sets cover a wide range of survey frequencies f_{surv} ranging from Hz to MHz, measurement directions with respect to the inherent anisotropy and prevailing pressure conditions (*in-situ* stress versus confining pressure). The *in-situ* stress state within the test volume was characterized prior to the stimulation experiments (Krietsch *et al.* 2019). In regions far away from the shear zones representing the unperturbed stress field, the stress tensor exhibited maximum and minimum principal stress magnitudes of ∼14 and ∼8.7 MPa, respectively. Wenning *et al.* (2018) also reports present-day low-pressure conditions at the GTS with minimum principal stress in the range of 8 to 12 MPa and maximum principal stress in the range of 13 to 17 MPa. Based on this information, we will use values from 8 to 17 MPa to select the data for comparison whenever a range of pressures is provided. Finally, we have taken into account other potential sources of discrepancies, such as saturation conditions, data repeatability and associated uncertainties. This approach is expected to ensure a robust foundation for our comparative analysis and interpretation. In the following, we

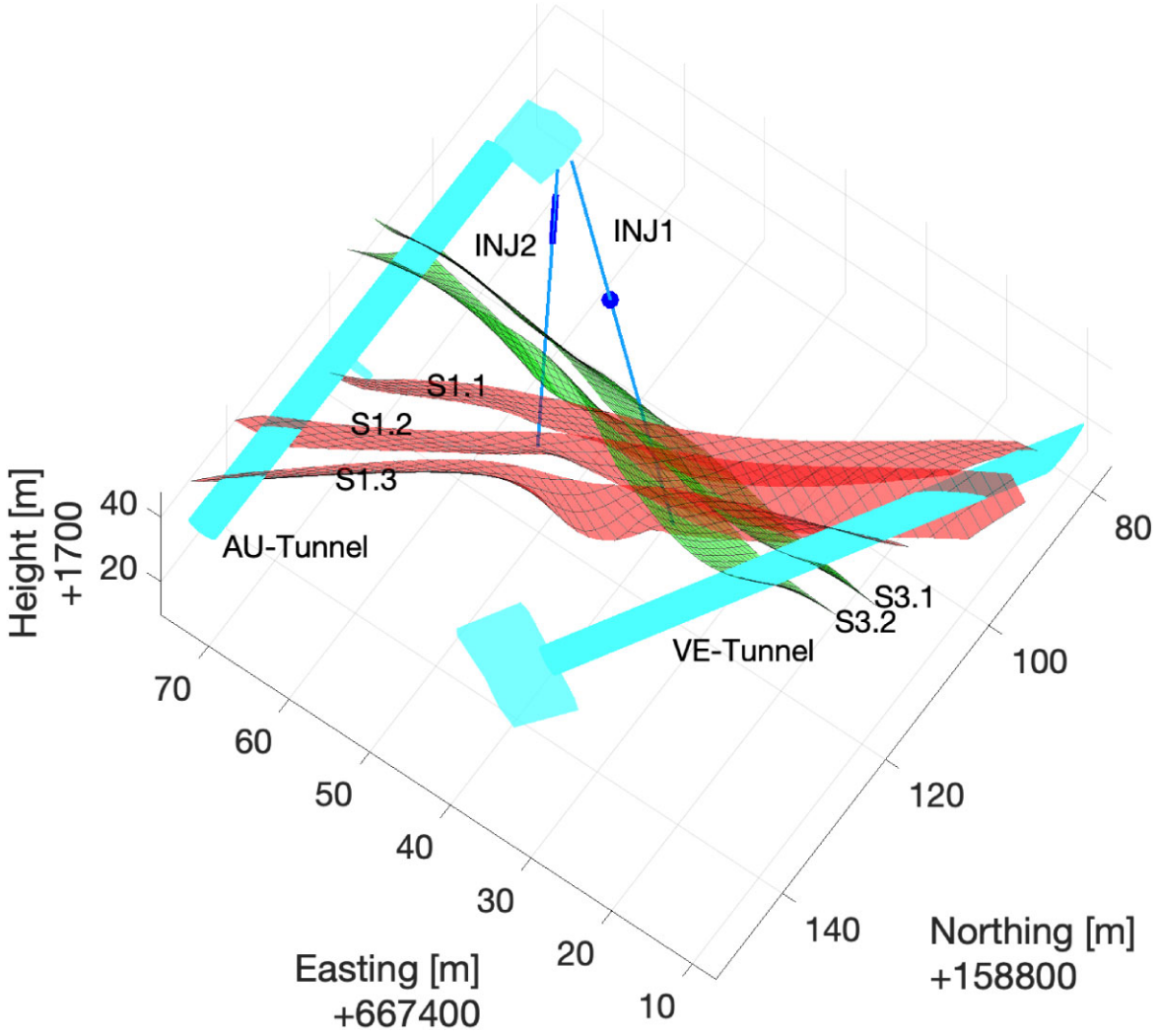

Figure 1. Locations of boreholes INJ1 and INJ2. The two boreholes intersect sub-vertical ductile shear zones (red and green structures). Some of these shear zones follow a NE-SW strike, classified as being of S1-type, and two an E-W strike, classified as being of S3-type. Between the two S3-type shear zones the rock mass is highly fractured. The part of the INJ2 borehole used for FWS log measurements in Barbosa *et al.* (2019) is illustrated as a blue line. The ultrasonic measurements were performed on samples extracted from INJ1 and their location is denoted by the blue circle. The FWS and ultrasonic measurements correspond to sections that were considered in previous works as a being representative of the local host rock (e.g. Barbosa *et al.* 2019, 2021).

present a short review the studies included in our analysis, sorted based on their characteristic survey frequency. Additional information from the reviewed studies are provided in Appendix A.

2.2 Near-surface survey from Holliger and Bühnemann (1996)

Holliger & Bühnemann (1996) reported Q_P-estimates based on borehole-to-tunnel seismic experiments conducted at the GTS. The Q_P-estimates were derived from the first cycles of transmitted P waves using the spectral ratio method (e.g. Tarif & Bourbie 1987) and assuming that both the velocity and Q_P remained frequency-independent within the prevailing spectral range (i.e. 50–1200 Hz). Regarding V_P, Holliger & Bühnemann (1996) considered a mean value of 5000 m s^{-1} to interpret their measurements. The values are assigned to a mean frequency of 625 Hz, which corresponds to the midpoint of the spectral ratio fitting range from 50 to 1200 Hz. The list of values, which are representative of the granodioritic host rock at GTS, along with standard deviations, is given in Table 1.

2.3 Near-surface survey from Doetsch et al. (2020)

As part of the ISC project, Doetsch *et al.* (2020) performed a seismic study involving both tunnel-to-tunnel and 3-D-type configurations to characterize the crystalline rocks at the GTS. To generate seismic signals, a sparker source was activated within six water-filled boreholes. The dominant frequency characterizing the first-arriving seismic energy was approximately 1.1 kHz.

Due to the foliation of the Grimsel granodiorite, the seismic velocities exhibit anisotropy (e.g. Wenning *et al.* 2018), and the authors assumed a transversely isotropic medium to model velocity anisotropy. Specifically, for v_0, the velocity in the direction normal to the anisotropy plane, they obtained a distribution of values due to the inhomogeneity of the rock within the probed volume and provided v_0 values for boreholes INJ1 and INJ2. We compute a mean velocity value and uncertainty for the less fractured shallow sections, which are more representative of the granodioritic host rock (Table 1). Finally, Q_P-values were not reported by Doetsch *et al.* (2020).

Table 1. Data reported for the Grimsel granodiorite and shown in Fig. 4, sorted according to their characteristic survey frequency $\bar{f}_{\mathrm{surv}}$. Mean values ($\bar{x}$) and associated uncertainties (Δx) in the variables Q_P^{-1}, V_P and f_{surv} are provided whenever possible. The annotations 'HF-ultrasonic', and 'LF-ultrasonic', and 'Tomography' distinguish the ultrasonic measurements with low- and high-frequency transducers, respectively, and the tomography results reported in Majer *et al.* (1990).

Work	$\bar{Q}_P^{-1}$	ΔQ_P^{-1}	$\bar{V}_P$	ΔV_P	$\bar{f}_{\mathrm{surv}}$	Δf_{surv}
Holliger & Bühnemann (1996)	0.0286	0.016	5000 m s^{-1}	100 m s^{-1}	625 Hz	575 Hz
Doetsch *et al.* (2020)	–	–	5200 m s^{-1}	102 m s^{-1}	1100 Hz	500 Hz
Majer *et al.* (1990) Tomography	0.067	0.0015	5200 m s^{-1}	115 m s^{-1}	7.5 kHz	2.5 kHz
Barbosa *et al.* (2019)	0.082	0.009	5180 m s^{-1}	20 m s^{-1}	19.0 kHz	1.5 kHz
Majer *et al.* (1990) LF-ultrasonic	–	–	5385 m s^{-1}	110 m s^{-1}	475 kHz	47.5 kHz
This work	0.053	0.007	5450 m s^{-1}	95 m s^{-1}	635 kHz	73 kHz
Majer *et al.* (1990) HF-ultrasonic	–	–	5485 m s^{-1}	210 m s^{-1}	900 kHz	90 kHz

2.4 Near-surface survey from Majer et al. (1990)

In the context of the Fracture Research Investigation (FRI) project at the GTS, Majer *et al.* (1990) conducted a series of multi-offset/multisource VSP experiments near the boundary between the Grimsel granodiorite and the Central Aaregranite. They performed a tomographic analysis using VSP and cross-hole data for multiple offsets and azimuths, with peak energy transmission occurring at frequencies between 5 and 10 kHz.

The travel times were used for a tomographic inversion while accounting for the known anisotropy of the rock to improve imaging results. Based on their anisotropy model, we computed the mean velocity and its uncertainty. To estimate attenuation, Majer *et al.* (1990) applied the same inversion procedure used for travel times to the first arrival amplitudes. The background rock attenuation was estimated by averaging the largest signal amplitudes after correcting for geometrical spreading and source radiation patterns. Table 1 shows the corresponding values for the inverse of the quality factor Q_P^{-1}.

2.5 FWS results from Barbosa et al. (2019)

Barbosa *et al.* (2019) analysed FWS log data acquired in a quasi-stationary way along borehole INJ2 (Fig. 1). Two nominal sonic source frequencies were considered, 15 and 25 kHz. A sonic *P*-wave phase velocity profile was computed along macroscopically intact borehole sections by comparing the phase spectra of signals recorded at two receivers. Given the proximity of the nominal source frequencies, both sets of measurements were used to estimate a mean value for V_P and f_{surv} while also providing an uncertainty estimate. Barbosa *et al.* (2019) further quantified different contributions to the sonic *P*-wave attenuation (geometrical spreading, fracture-related scattering, intrinsic attenuation) using the spectral ratio method. We consider their intrinsic host rock attenuation estimates for the least fractured section of INJ2 (Table 1).

2.6 Ultrasonic measurements from Majer et al. (1990)

Majer *et al.* (1990) conducted ultrasonic experiments on macroscopically intact rock specimens extracted from a borehole of the FRI project. Two sets of transducers were used, operating at approximately 475 and 900 kHz for *P*-wave propagation, referred to as the 'low-' and 'high-frequency' transducers, respectively. Our focus is on results obtained under saturated conditions for *P* waves at pressures comparable to the GTS *in-situ* stress field. *P*-wave velocities and peak-to-peak amplitudes of the initial arrivals were computed from recorded waveforms. For each source frequency data set, we determined a mean *P*-wave velocity value and its standard deviation over a pressure range representative of GTS conditions. While the authors qualitatively analysed amplitude decay using peak-to-peak amplitudes, they did not report Q_P values for the experiments. The extracted velocity values for low- and high-frequency measurements are listed in Table 1 as 'LF-ultrasonic' and 'HF-ultrasonic', respectively.

2.7 This work: ultrasonic measurements performed on samples from borehole INJ1

To complement the data previously described in this section, we have performed pressure-dependent ultrasonic measurements of *P*- and *S*-wave arrivals in rock samples from the INJ1 borehole at the GTS, Fig. 1. The samples were obtained from a core representative of macroscopically intact sections of the GTS boreholes and are thus regarded as being representative of the Grimsel granodioritic host rock (e.g. Wenning *et al.* 2018; Barbosa *et al.* 2019, 2021). The core was retrieved at a distance between 16 and 16.25 m from the top of INJ1 borehole and the ultrasonic measurements were taken on two plugs extracted from this core. Due to the absence of visible fractures, the ultrasonic measurements are expected to be comparable with those described in Section 2.6 and provide the missing attenuation information in the megahertz range.

The data analysis workflow and methodological details are outlined in Appendix B. We measured *P*- and *S*-wave arrivals using the pulse transmission technique under confining pressures up to ∼50 MPa. The resonance frequency of the transducers was set to 1 MHz. We considered samples with two different lengths, equal to 5.87 and 7.34 cm, hereafter referred to as L_1 and L_2, respectively.

Fig. 2 shows the resulting group *P*- and *S*-wave velocities as functions of (i) confining pressure, (ii) saturation condition (i.e. dry and water-saturated) and (iii) sample length. Group velocities were computed at the peak frequency in the amplitude spectrum of the signal propagating through the sample (Appendix B). *P*-wave velocities under dry conditions exhibit a very similar pressure-dependence and magnitudes. Conversely, *P*-wave velocities under saturated conditions exhibit a less consistent behaviour at low confining pressures, which could be due to a partial saturation of the sample's pore space during the ultrasonic acquisition. *S*-wave velocities, which could only be reliably obtained under dry conditions (Appendix B), exhibit a consistent pressure dependence.

Fig. 3 shows the *P*- and *S*-wave attenuation obtained using the frequency shift method (Quan & Harris 1997) as functions of confining pressure, saturation condition and sample length. The *P*-wave attenuation under dry conditions exhibits higher values than under saturated conditions as well as a more prominent pressure dependence for confining pressures above 15 MPa. Under dry conditions,

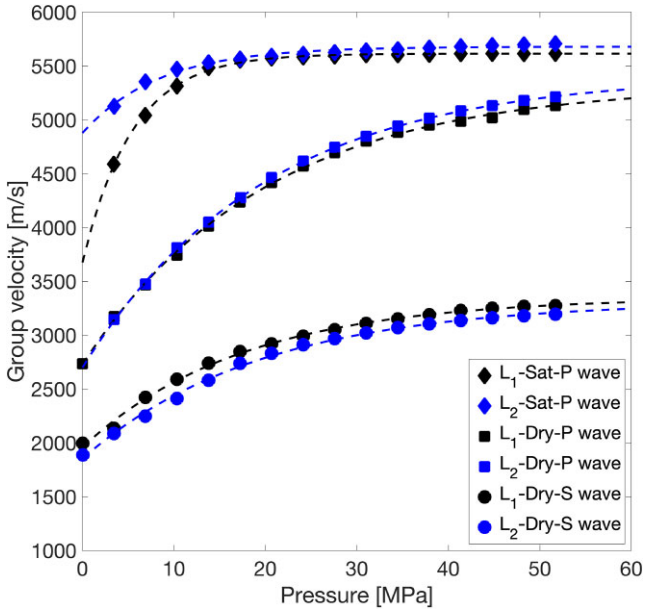

Figure 2. Pressure dependence of *P*- and *S*-wave ultrasonic velocities of the Grimsel granodiorite. Samples were extracted from borehole INJ1 (Fig. 1). Different symbols denote different combinations of saturation conditions, sample length and wave mode. Dashed lines correspond to the fitting curves obtained using eq. (9) from Shapiro (2003) to model the pressure dependence of *P*- and *S*-wave velocities under dry and saturated conditions (see Section 4 for a detailed discussion).

the pressure dependence of *P*- and *S*-wave attenuation shows less consistency compared to group velocities (Fig. 2), implying a higher sensitivity to crack-related effects. *S*-wave attenuation is similar in magnitude between both samples and comparable to *P* waves. Interestingly, all attenuation values converge to a consistent non-zero asymptotic value at high confining pressures, where crack-related effects are expected to be minimal.

Table 1 lists the mean and standard deviation of the *P*-wave attenuation and velocity as well as the corresponding survey frequency obtained from these ultrasonic experiments. Only measurements obtained under saturated conditions and for confining pressures representative of the GTS *in-situ* stress field (8 to 17 MPa) are considered. There are three confining pressures that are within this range (10.3, 13.8 and 17.2 MPa). Finally, to compute the statistical quantities, we consider a single data set composed by the measurements for samples L_1 and L_2 together.

3 FREQUENCY-DEPENDENT ATTENUATION AND VELOCITY OF THE GRIMSEL GRANODIORITE

Fig. 4 presents the main result of this work, which is the set of *P*-wave velocity and attenuation values reviewed in Section 2 as a function of their survey frequency (Table 1). We also include the values derived in this work for *P* waves under water-saturated conditions (Section 2.7). Both the *P*-wave attenuation and velocity values exhibit a consistent frequency-dependent behaviour, which aligns with the typical Kramers–Kronig causal relation predicted by viscoelastic models (e.g. Carcione 2007). That is, peak attenuation values tend to coincide with maximal velocity dispersion.

Various mechanisms could potentially explain the dynamic response observed in Fig. 4. Some of these mechanisms were described and compared for different rock types by Sarout (2012):

(i) Biot's intrinsic mechanism, which relates to the combined effect of fluid pressure gradients between the peaks and troughs of the seismic wave and the accelerations induced by the passing wavefield, producing relative fluid displacements at the wavelength scale. The associated viscous dissipation is observed as seismic attenuation and dispersion, which is maximal around Biot's critical frequency f_{Biot} (e.g. Müller *et al.* 2010)

$$f_{\text{Biot}} = \frac{\eta\phi}{2\pi\rho_f\kappa\tau}, \tag{1}$$

where η_f and ρ_f are the fluid viscosity and density, respectively, ϕ is the porosity, κ the permeability and τ the tortuosity. A lower bound for f_{Biot} can be obtained assuming an upper bound for permeability for the granodioritic host rock in the order of 10×10^{-19} m^2, a lower porosity bound in the order of 0.4 per cent following the reported values from Wenning *et al.* (2018) and an upper bound for τ equal to 1. For water, with a viscosity η_f of 10^{-3} Pa·s and density of 1000 Kg m^{-3}, we obtain that f_{Biot} is higher than 600 MHz, which is well beyond the frequency range in Fig. 4.

(ii) Scattering when seismic wavelengths become comparable to the characteristic size of the heterogeneities in the rock. Note that in this work, heterogeneities are only expected at the microscale. While the measurements were conducted at different scales (e.g. tunnel, cross-hole and laboratory), which could lead to varying influences from fractures and faults within the probed volume, we have carefully selected data representative of the less damaged regions free of macroscopic fractured within the studied volume. This ensures that the measurements are representative of macroscopically intact portions of the rock, thus, allowing us to rule out scattering and WIFF at the mesoscale as the primary causes of frequency-dependent attenuation and dispersion. On the other hand, the characteristic frequency at which scattering effects due to the presence of microcracks become relevant is given by (e.g. Sarout 2012)

$$f_{\text{Scattering}} = \frac{V_P}{2\pi 20R}, \tag{2}$$

where $2R$ is a characteristic size for the heterogeneities. Laboratory ultrasonic testing (MHz range) on crystalline rock samples is expected to lie in the scattering regime for $R > 10^{-4}$ m (Sarout 2012). While there are no visible cracks in the samples, one must take this mechanism into account when analysing the effects at ultrasonic frequencies.

(iii) Conversely, Sarout (2012), pointed out that the microcrack-related WIFF phenomenon known as squirt flow is expected to be the main contributor to seismic dispersion and attenuation observed around sonic frequencies in fluid-saturated crystalline rocks. This mechanism involves viscous dissipation resulting from flow within or between pores and cracks with different shapes or orientations, triggered by wave-induced strains (e.g. Winkler & Nur 1979; de Paula *et al.* 2012). Indeed, the pressure dependence observed in our ultrasonic attenuation and velocity estimates, as well as in those of Majer *et al.* (1990), strongly suggest the presence of compliant microcracks. While several theoretical squirt flow models have been proposed, the main characteristics of the frequency dependence of velocity and attenuation associated with this phenomenon can be predicted using the phenomenological WIFF model by Johnson *et al.* (1987). In the following, we describe this model and the strategy employed to fit the data plotted in Fig. 4.

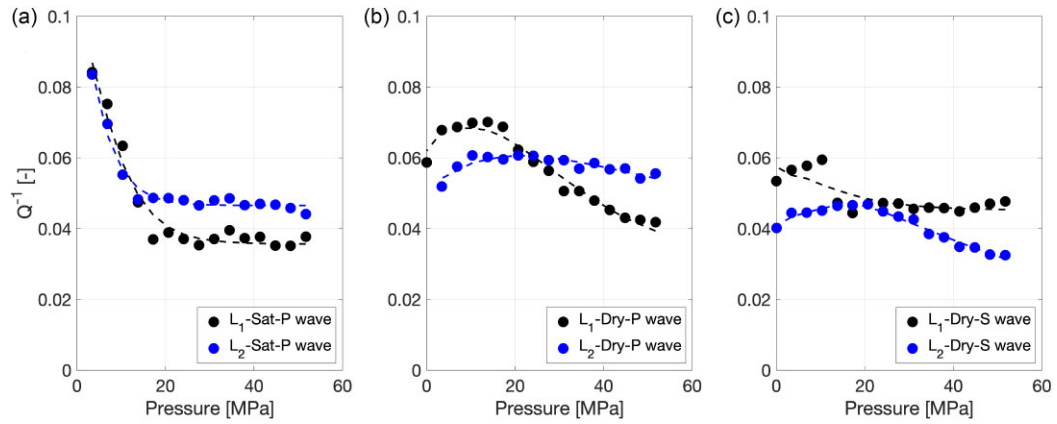

Figure 3. *P*- (a, b) and *S*-wave (c) attenuation of the Grimsel granodiorite inferred from ultrasonic measurements as functions of confining pressure on samples L_1 and L_2 from borehole INJ1 (Fig. 1). Panels (a) and (b) correspond to water-saturated and dry *P*-wave measurements, respectively. Different colours denote different sample lengths. Dashed lines correspond to the fitting curves obtained using eq. (17) from Meglis *et al.* (1996) to model the pressure dependence of *P*-wave attenuation under dry and saturated conditions (see Section 5 for a detailed discussion).

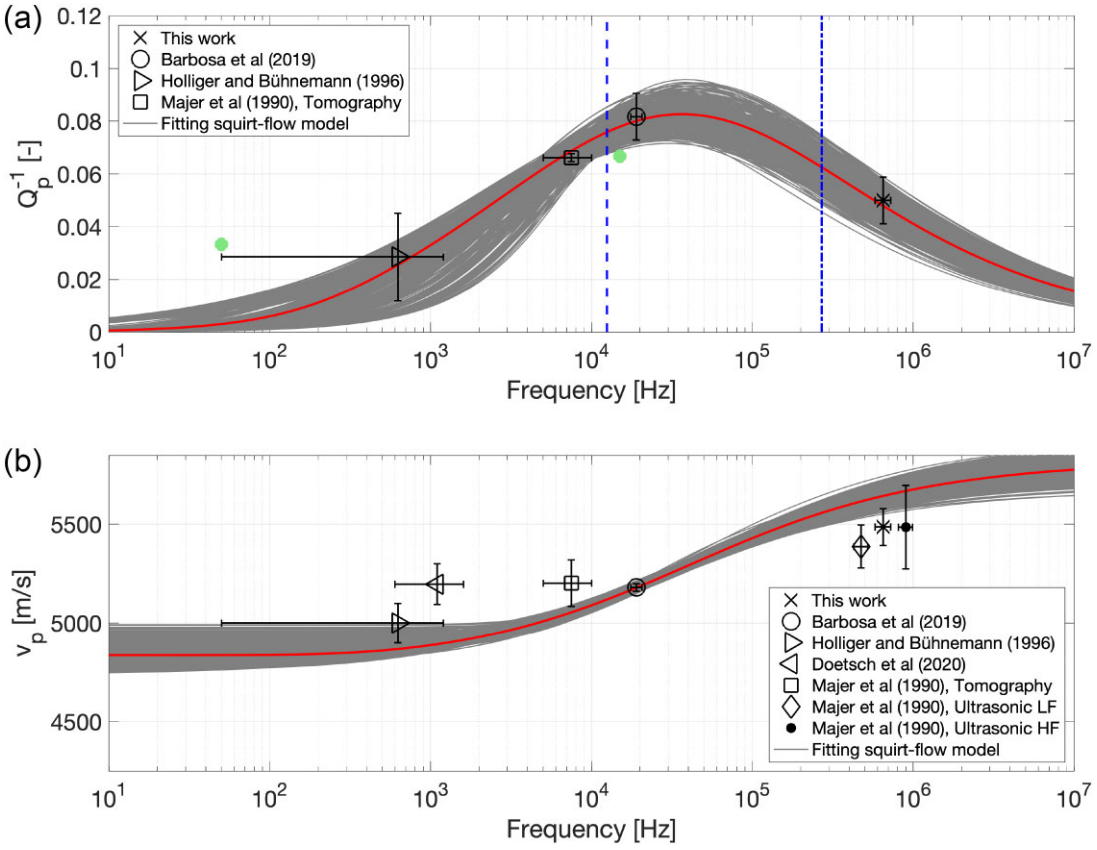

Figure 4. *P*-wave (a) attenuation and (b) velocity measurements from various surveys characterizing the Grimsel granodiorite as a function of the survey frequency. The values are detailed in Table 1. The grey curves represent the fitting result outlined in Section 3.1, using pseudo-randomly generated data sets from the mean values and uncertainties in Table 1. We conducted this fitting procedure 500 times. The red curve illustrates the model response when using the mean parameter values derived from these 500 individual sets of fitting parameters. Vertical blue lines indicate the predicted squirt flow characteristic frequency inferred independently from our pressure-dependent ultrasonic velocities. Green dots correspond to attenuation values reported by Li & Richwalski (1996) for the crystalline rocks of the KTB deep drilling site.

3.1 A phenomenological WIFF model for frequency-dependent attenuation and velocity

Due to its simplicity and accuracy, a widely used model to describe *P*-wave attenuation and velocity dispersion due to WIFF effects employs a complex-valued, frequency-dependent *P*-wave modulus $H_{sf}(\omega)$ given by (e.g. Johnson *et al.* 1987; Gurevich *et al.* 2009; Guo *et al.* 2017)

$$H_{sf}(\omega) = H_{HF}\left[1 + \left(\frac{H_{HF} - H_{LF}}{H_{LF}}\right) \Big/ \left(1 - \zeta + \zeta\sqrt{1 - i\frac{\omega}{\omega_{sf}\zeta^2}}\right)\right]^{-1}, \quad (3)$$

where H_{LF} and H_{HF} are the saturated P-wave moduli in the low- and high-frequency limits, respectively, and ζ and ω_{sf} are the parameters defining the shape and characteristic frequency of the frequency dependence of $H_{sf}(\omega)$, respectively. The characteristic frequency, at which velocity dispersion and attenuation are maximal, occurs approximately when $\omega = \omega_{sf}$. The parameter ζ is often associated with the type of distribution of the cracks, going towards zero as the randomness of the spatial and/or size distribution increases. The so-called branching function approach given by eq. (3) is very convenient because it describes the fluid-pressure relaxation process behind WIFF through a phenomenological viscoelastic concept (e.g. Bardet 1992), while its parameters can still be interpreted in terms of rock physical properties. An advantage over other popular theoretical models (e.g. Maxwell, Voigt, Zener) is that the branching-function approach satisfies causality and respects the asymptotic behaviors at low and high frequencies predicted by rock physics models.

Using eq. (3), we can compute the associated frequency-dependent P-wave velocity $V_{sf}(\omega)$ and attenuation $Q_{sf}^{-1}(\omega)$ as (Carcione 2007)

$$V_{sf}(\omega) = \left[\Re\left(\frac{1}{V_c(\omega)}\right)\right]^{-1},$$
$$Q_{sf}^{-1}(\omega) = \frac{\Im[V_c(\omega)^2]}{\Re[V_c(\omega)^2]}, \tag{4}$$

with $V_c(\omega) = \sqrt{H_{sf}(\omega)/\rho}$ and ρ being the bulk density.

To find the optimal parameters describing the observations in Fig. 4, we minimize an objective function given by the weighted L^2-norms of the discrepancies between the observed P-wave velocities V_{obs} and attenuation Q_{obs}^{-1} with those predicted using eqs (3) to (4)

$$F(H_{HF}, H_{LF}, \zeta, \omega_{sf}) = \sqrt{\sum_{k=1}^{NV}\left|\frac{V_{\text{obs},k} - V_{sf,k}}{\Delta V_{\text{obs},k}}\right|^2} + \sqrt{\sum_{k=1}^{NQ}\left|\frac{Q_{\text{obs},k}^{-1} - Q_{sf,k}^{-1}}{\Delta Q_{\text{obs},k}^{-1}}\right|^2}, \tag{5}$$

where NV and NQ are the number of velocity and attenuation observations, respectively (Fig. 4). In addition, $\Delta V_{\text{obs},k}$ and $\Delta Q_{\text{obs},k}^{-1}$ denote the uncertainties associated with each observation. The weighted least-squares objective function in eq. (5) normalizes the differences between observed and predicted data by their respective uncertainties. In doing so, we ensure that data points with lower uncertainties have a greater influence on the fitting process, which, in turn, leads to a tighter fit for more reliable observations. In total, we have 4 unknown model parameters (i.e. H_{HF}, H_{LF}, ζ and ω_{sf}) and 11 known values of velocity and attenuation (Table 1).

To account for the observation uncertainties, pseudo-random data sets were generated based on the mean values and uncertainties given in Table 1 as follows

$$x = \bar{X} + rand \cdot \Delta X, \tag{6}$$

where x denotes V_P, Q_P^{-1}, f_{surv}, $\bar{X}$ and ΔX the corresponding mean values and standard deviations, respectively. $rand$ is a uniformly distributed pseudo-random number between -1 and 1. Each data set (i.e. 11 data values generated using eq. 6) was then fitted using eq. (5) to obtain a model solution. This fitting process was performed on 500 different data sets. The statistics of each model parameter is shown in Table 2. Fig. 4 shows the resulting 500 fitting models (grey curves) and a model solution computed using the mean values of each model parameter (red curve). Despite the diversity in survey frequencies, techniques and conditions underlying each observation, the fitting results exhibit a remarkably good agreement with the WIFF model.

Table 2. Statistics of fitting parameters of P-wave attenuation and velocity under water-saturated conditions using eqs (3) to (5).

	Mean value	Standard deviation
H_{HF} (GPa)	92.6	1.7
H_{LF} (GPa)	63.8	1.45
ζ (−)	0.09	0.11
ω_{sf} (s^{-1})	1.79e5	3.7e4

In the following section, we examine in more detail the pressure-dependent ultrasonic data collected in the framework of this study to independently estimate certain parameters of the model of Johnson *et al.* (1987). By comparing these estimates with the parameters derived from the fitting process, we can assess their physical validity.

4 SQUIRT FLOW MODEL PARAMETERS DERIVED FROM PRESSURE-DEPENDENT ULTRASONIC DATA

In this section, we aim to infer rock and crack properties based on the observed pressure dependence of the velocity and attenuation (Figs 2 and 3) that are relevant for the interpretation of the fitting model shown in Fig. 4. This will help us to assess to what extent a crack-related squirt flow mechanism could explain the observed seismic attenuation and dispersion behaviour of the Grimsel granodiorite.

In particular, we aim at inferring the characteristic frequency ω_{sf} of the WIFF process using the pressure-dependent ultrasonic measurements. Gurevich *et al.* (2010) derived an expression to obtain ω_{sf} assuming liquid saturation as

$$\omega_{sf}(P) = \frac{8\xi_c^2 K_{\text{dry}}^0}{3\eta_f \Theta_c}\left[\frac{K_{\text{dry}}^0}{K_{\text{dry}}(P)}\right]^{1/2}, \tag{7}$$

which depends on the crack aspect ratio ξ_c, a parameter Θ_c quantifying the sensitivity of the elastic moduli to the differential stress and the dry bulk moduli of the rock at pressure of interest P and in the hypothetical case of absence of cracks, $K_{\text{dry}}(P)$ and K_{dry}^0, respectively. It is important to mention that eq. (7) is compatible with the conceptual crack distribution model of Shapiro (2003). Thus, we first follow the approach presented by Shapiro (2003) and use the P- and S-wave velocity dependence on the confining pressure under dry conditions to get Θ_c and K_{dry}^0. We then proceed to estimate ξ_c, which is the other crack-related parameter in eq. (7), using the water-saturated P-wave measurements. Note that $K_{\text{dry}}(P)$ can be derived from P- and S-wave velocities under dry conditions at a given pressure P.

4.1 Velocity under dry conditions: estimating Θ_c and K_{dry}^0

The pressure dependence of both P- and S-wave velocities under dry and saturated conditions can be well approximated by the following relationship (Shapiro 2003)

$$V(P) = A + KP - B\exp(-PD), \tag{8}$$

where $P = P_c - P_p$ is the differential stress between the confining pressure P_c and the pore pressure P_p. The latter is negligible in our experiments. The coefficients A, K, B, D are fitting parameters.

Table 3. Fitting parameters in eq. (9) and inferred Θ_c for the crack distribution using *P*- and *S*-wave data under dry conditions for samples L_1 and L_2.

	P-L_1	P-L_2	S-L_1	S-L_2
A (m s^{-1})	5326	5419	3352	3312
B (m s^{-1})	2600	2721	1394	1460
D (GPa^{-1})	50.28	50.36	56.98	51.40
Θ_c (−)	1902	1906	1727	1558

Eq. (8) provides a phenomenological explanation for the pressure dependence in a porous and/or cracked medium by the closure of both stiff (related to the K-term) and compliant (related to the B-term) pores and/or cracks in a phenomenological way (de Paula *et al.* 2012). Furthermore, Shapiro (2003) argues that the contribution of K is in general much smaller than that of the other parameters, which implies that the relationship can be simplified to

$$V(P) = A - B\exp(-PD). \tag{9}$$

Fig. 2 shows the fitting results (dashed lines) for *P*- and *S*-wave velocities under dry conditions using eq. (9). The corresponding fitting parameters are given in Table 3.

Shapiro (2003) showed that in the case of *P* waves, the coefficient D in eq. (9) is $D_{P\text{wave}} = \Theta_c K^0_{\text{dry}}$, with

$$\Theta_c = \frac{1}{C^0_{\text{dry}}}\frac{\partial C_{\text{dry}}}{\partial \phi_c}\bigg|_{\phi_c=0}, \tag{10}$$

where $C^0_{\text{dry}} = 1/K^0_{\text{dry}}$, $C_{\text{dry}}(P) = 1/K_{\text{dry}}(P)$ and ϕ_c is the compliant porosity. As mentioned when describing eq. (7), the dimensionless quantity Θ_c defines the sensitivity of the elastic moduli to the differential stress also referred to as elastic piezosensitivity (Shapiro 2003). We extend the computation of Θ_c based on *S*-wave velocities as $D_{S\text{wave}}/\mu^0_{\text{dry}}$, with μ^0_{dry} being the dry-rock matrix shear modulus when $\phi_c = 0$. In Table 3, we show the Θ_c values computed from the fitting of P- ($\Theta_c = D_{P\text{wave}}/K^0_{\text{dry}}$) and *S* waves ($\Theta_c = D_{S\text{wave}}/\mu^0_{\text{dry}}$).

To estimate values of K^0_{dry} and μ^0_{dry}, we consider the high-pressure asymptotic velocity values quantified by the fitting parameter A in eq. (9) (Table 3) and the relation between elastic moduli and velocities. Furthermore, we average the results for both sample lengths considered

$$\mu^0_{\text{dry}} = \frac{1}{NL}\sum_i (A_{S\text{wave},i})^2\rho,$$
$$K^0_{\text{dry}} = \frac{1}{NL}\left[\sum_i (A_{P\text{wave},i})^2\rho\right] - 4/3\mu_{\text{dry}}, \tag{11}$$

where $i = (L_1, L_2)$ and $NL = 2$. Following Wenning *et al.* (2018), we use $\rho = 2730$ Kg m^{-3}, which was in agreement with our estimates based on Archimedes density method using weight and volume measurements.

By following the procedure described above, we obtained values of K^0_{dry} and μ^0_{dry} equal to 37.8 and 30.3 GPa, respectively. Overall, the parameters estimated from our dry sample measurements are reasonable as (i) the values for $D_{P\text{wave}}$ and $D_{S\text{wave}}$ are roughly equal and in good agreement with the typically reported values (Shapiro 2003; de Paula *et al.* 2012); (ii) Θ_c obtained from the fitting of the pressure dependence of both *P* and *S* waves is in the order of 1×10^3, which is within the realistic range of the orders of the piezosensitivity for rocks of 10^2-10^4 suggested by Shapiro (2003). For completeness, we have also considered eq. (8) to fit the velocities and found that $K_{P\text{wave}}$ and $K_{S\text{wave}}$ measured in MPa are of the order of 1 as demonstrated by Shapiro (2003), which implies that this term associated with the closure of stiff pores can be neglected.

Given that Θ_c and K^0_{dry} have been confidently estimated, we can now proceed to estimate ξ_c, which is the additional parameter necessary to compute the expected characteristic frequency of the microcrack-related WIFF process (eq. 7).

4.2 Velocity under saturated conditions: estimating ξ_c

So far, we have only considered velocities under dry conditions and modeled their pressure dependence. The latter is comparable for both *P* and *S* waves and points to the presence of compliant porosity that leads to a pressure sensitivity of the elastic properties of the samples. In the following, we consider the relation between *P*-wave velocities obtained under water-saturated and dry conditions to estimate the additional crack parameter ξ_c in eq. (7). Given the relatively high frequencies used in the ultrasonic experiments, we assume that the saturated measurements are representative of seismic signals falling within the unrelaxed regime (i.e. cracks behave as hydraulically isolated). More advanced approaches may be required for intermediate frequencies between the relaxed and unrelaxed regimes (e.g. Sun & Gurevich 2020).

Following Adelinet *et al.* (2011), we assume a distribution of randomly oriented spheroidal cracks with the crack density d_c and effective aspect ratio ξ_c defined as

$$d_c = \frac{1}{V}\sum_{i=1}^{n_c} a_i^3,$$
$$\xi_c = \frac{b}{a}, \tag{12}$$

where b and a are the lengths of the spheroid semi-axes, V is the volume of the sample and n_c the number of cracks. According to this model, a parameter δ_c can be used to characterize the coupling between matrix compliance, fluid compressibility and crack geometry under saturated conditions

$$\delta_c = \frac{E_0\pi\xi_c}{4(1-\nu_0^2)}\left(\frac{1}{K_f} - \frac{1}{K_0}\right), \tag{13}$$

where E_0, K_0 and ν_0 represent elastic parameters when ϕ_c=0, respectively the Young modulus, the bulk modulus and the Poisson ratio and K_f is the fluid bulk modulus.

In the saturated case, the effective normal compliance of a crack is changed due to fluid saturation and the parameter δ_c should be taken into account to estimate the saturated bulk K^{sat}_{HF} and shear moduli μ^{sat}_{HF}

$$\frac{K_0}{K^{\text{sat}}_{HF}} = 1 + d_c\frac{16(1-\nu_0^2)}{9(1-2\nu_0)}\left(\frac{\delta_c}{1+\delta_c}\right),$$
$$\frac{\mu_0}{\mu^{\text{sat}}_{HF}} = 1 + d_c\left[\frac{16(1-\nu_0)}{15(1-\frac{\nu_0}{2})} + \frac{32(1-\nu_0)}{45}\left(\frac{\delta_c}{1+\delta_c}\right)\right], \tag{14}$$

with μ_0 being the shear modulus of the free-inclusion matrix.

Note that the dry moduli K_{dry} and μ_{dry} can be deduced from eq. (14) using that $K_f \to 0$ and thus $\delta_c \to \infty$ and $\frac{\delta_c}{1+\delta_c} \to 1$. As a result, we get (e.g. Guéguen & Sarout 2011)

$$\frac{K^0_{\text{dry}}}{K_{\text{dry}}} = 1 + d_c\frac{16(1-\nu_0^2)}{9(1-2\nu_0)},$$
$$\frac{\mu^0_{\text{dry}}}{\mu_{\text{dry}}} = 1 + d_c\frac{32(1-\nu_0)(5-\nu_0)}{45(2-\nu_0)}. \tag{15}$$

Since eq. (15) are independent from ξ_c, we can obtain the crack density d_c directly using the P- and S-wave velocities measured at dry conditions. It is important to mention that we do not assume that K_0 and $K^0_{\rm dry}$ are equal in eqs (14) and (15) as the frame surrounding the cracks may include non-closable pores that change their stiffness with saturation (e.g. Li *et al.* 2018), leading to potential differences in the frame elastic moduli under dry and saturated conditions. We also assume that eq. (15), which represents an approximation derived assuming effective isotropy, is valid despite the well-known intrinsic anisotropy of the Grimsel granodiorite.

In Fig. 5(a), we show the crack density d_c (eq. 15) obtained using the known values of $K^0_{\rm dry}$ and $\mu^0_{\rm dry}$ (eq. 11) and the values of $K_{\rm dry}$ and $\mu_{\rm dry}$ computed from the dry P- and S-wave velocities as functions of pressure. Given that eq. (15) allow to compute crack densities using either $K_{\rm dry}$ or $\mu_{\rm dry}$, we have computed the average between both values for each confining pressure. Overall, we observe that the inferred pressure-dependent crack density d_c for samples L_1 and L_2 is consistent (Fig. 5a). Note that while the inverted crack density values at low pressures appear relatively high, they remain within the expected range for the employed Non-Interactive Approximation model. This approach predicts diminishing reductions in elastic moduli with increasing crack density, which can lead to an overestimation of inverted crack densities, sometimes even exceeding values of 1 (e.g. Nasseri *et al.* 2009; Pimienta *et al.* 2019). Conversely, the model is expected to remain realistic and robust for crack densities up to 0.5 (e.g. Kachanov 1992; Nasseri *et al.* 2009), which indicates that our results for Grimsel *in situ* conditions are within a valid range. At lower pressures, however, the uncertainty in the inversion increases, making the interpretation of very high crack densities correspondingly less robust.

Based on eq. (14), we can invert for K_0 and the effective aspect ratio ξ_c using the observed P-wave velocities under saturated conditions and the known values of d_c at each pressure. Given that we do not have S-wave velocities measured under saturated conditions, we assume that μ_0 is equal to $\mu^0_{\rm dry}$, which was obtained from the fitting the dry S-wave velocities (eq. 11). The minimization function is based on the L^2-norm of the discrepancies between the observed P-wave velocities under saturated conditions V_P and those predicted using eq. (14) ($V_{P,\rm model} = \sqrt{\frac{K^{\rm sat}_{HF} + 4\mu^{\rm sat}_{HF}/3}{\rho}}$)

$$F(K_0, \xi_c) = \sqrt{\sum_{k=1}^{NP} |V_P^k - V_{P,\rm model}^k|^2}. \quad (16)$$

In eq. (16), the superscript k denotes the k-th confining pressure and NP the total number of confining pressures considered. We assume that $K_f = 2.25$ GPa.

As a result of minimizing eq. (16), we obtain the P-wave velocities shown in Fig. 6. The agreement with respect to the observed velocities is very good for the two samples considered. The optimal values of K_0 and ξ_c are given in Table 4 for both samples. The inferred values are reasonable as (i) ξ_c obtained from the fitting of the pressure dependence of both P and S waves is in the order of 1×10^{-3}, which is below the threshold value of 0.01 for compliant porosity (Shapiro 2003) and within the range of typical values (de Paula *et al.* 2012; Li *et al.* 2018); (ii) the crack porosity ϕ_c, which can be computed as $\frac{4}{3}\pi d_c \xi_c$ for a spheroidal crack population (Adelinet *et al.* 2011), is consistent with Wenning *et al.* (2018), which indicated that $\phi < 0.01$ above 30 MPa (Fig. 5b) and that the porosity prevails mainly between grain contacts (i.e. intergranular micropores); (iii) the saturated-frame P-wave modulus ($K_0 + 4/3\mu_0$) obtained for samples L_1 and L_2 is equal to 90.1 and 89.9 GPa, respectively. These values are in excellent agreement with the H_{HF} value derived from fitting the data shown in Fig. 4 (see Table 2).

Finally, we can compute ω_{sf} (eq. 7) for the samples L_1 and L_2 using the aspect ratio ξ_c values given in Table 4, Θ_c given in Table 3, $K^0_{\rm dry}$ computed using eq. (11) and $K_{\rm dry}(P)$ derived from P- and S-wave velocities under dry conditions and averaging values corresponding to pressures between 8 and 17 MPa. Assuming a water viscosity η_f of 10^{-3} Pa·s, we obtain values of $f_{sf} = \omega_{sf}/2\pi$ of 282 and 12.8 kHz for samples L_1 and L_2, respectively (blue lines in Fig. 4).

The values of f_{sf} are within the expected range (1 kHz to 1 MHz) for the squirt flow mechanism (e.g. Guéguen & Sarout 2011). Note that the main source of discrepancy between the two characteristic frequencies is the aspect ratio considered. Interestingly, the effective characteristic frequency obtained by fitting the data with the model of Johnson *et al.* (1987) lies between the two frequencies independently estimated from our ultrasonic measurements. This indicates that, as hypothesized, squirt flow is a plausible mechanism behind the frequency-dependent attenuation and velocity of seismic waves exhibited by the Grimsel granodiorite. At the prevailing *in-situ* stresses, the presence of fluid-saturated cracks at the grain scale results in a frequency-dependent seismic response. At low frequencies, such as those typically used in exploration seismics, the pressure induced by the passing wave has time to equilibrate throughout the pore space. This is referred to as the relaxed limit. On the other hand, at ultrasonic frequencies, the pore pressure has no time to equilibrate during the passage of the wave, thus, making the fluid stiffening effect in the cracks maximal, which is denoted as the unrelaxed limit. At this limit, we measure the stiffest response of the rock for any given saturation conditions. At intermediate frequencies, such as the ones prevailing in sonic logs or near-surface seismics, there will be pressure gradients between pores and/or cracks, whose equilibration produces maximal attenuation and velocity dispersion in the passing waves.

5 DISCUSSION

5.1 Origin of microcracks at GTS

The diversity of the data base analysed in this study and the internal consistency of the inferred WIFF model suggest pervasive microcracking throughout the GTS. Indeed, widespread observations of seismic velocities indicate that the presence of cracks in the Earth's crystalline crust is ubiquitous (e.g. Christensen & Mooney 1995; Crampin & Gao 2010). Regarding the origin of the microcracks in the crystalline rocks at GTS, a plausible explanation may be linked to the ductile-brittle deformation during the late stage of the Alpine orogeny and through the exhumation of the Aar Massif, where the GTS is located. Under this scenario, pervasive microcracking can form as rocks are subjected to pressures and temperatures lower than those at which they crystallized. At the grain scale, internal stresses arise due to mismatches in the elastic and thermoelastic properties of adjacent grains (e.g. Anders *et al.* 2014).

In this regard, Wenning *et al.* (2018) characterized the elastic and fluid flow properties within and around fault zones intersected by ISC boreholes at the GTS. They found that rock porosity primarily occurs at grain contacts and is strongly influenced by ductile deformation. Microscopic observations reveal maximum crack apertures in the micrometer range (Möri *et al.* 2021), which, according to our aspect ratio estimates, suggest that grain boundary lengths are in

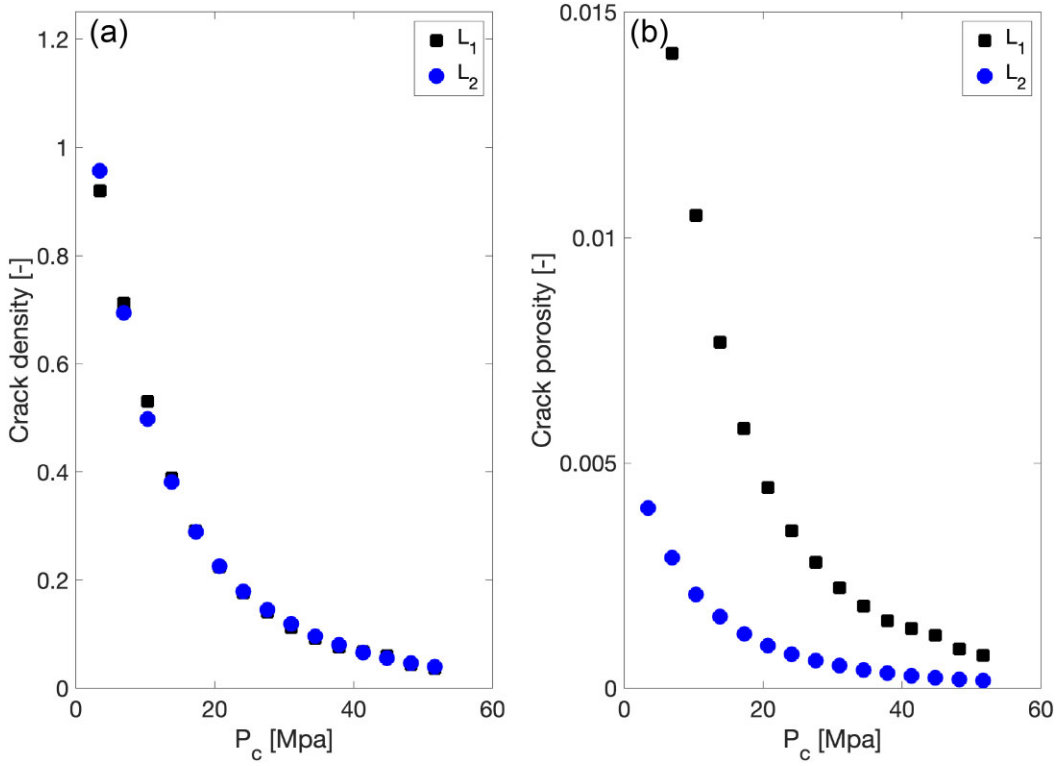

Figure 5. Effective (a) crack density and (b) porosity obtained from *P*- and *S*-wave ultrasonic measurements as a function of confining pressure. Crack densities d_c were obtained using eq. (15) and the *P*- and *S*-wave velocities shown in Fig. B9. Crack porosities ϕ_c were computed as $\frac{4}{3}\pi d_c \xi_c$.

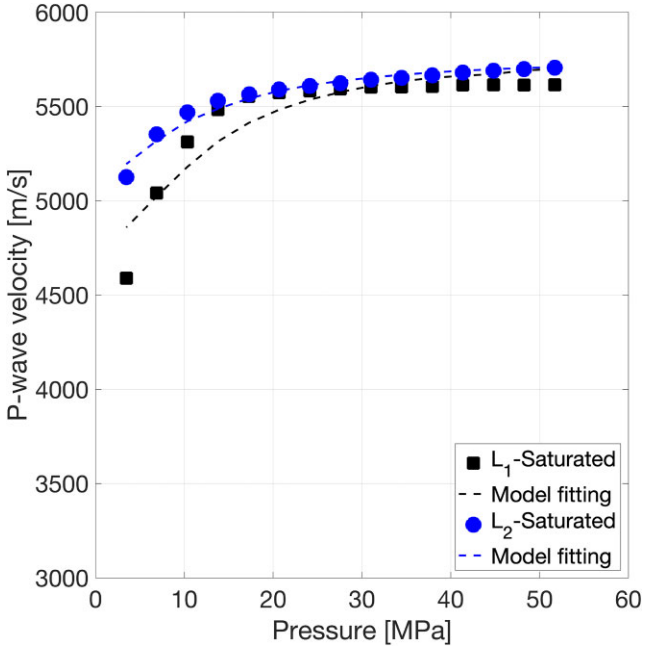

Figure 6. Comparison between measured *P*-wave velocities measured under saturated conditions (same as those shown in Fig. 2) and the ones inferred using eq. (14).

Table 4. Fitting parameters of K_0 and ξ_c in eq. (14) inferred from *P*-wave velocities measured under saturated conditions.

	Sample L_1	Sample L_2
K_0 (GPa)	49.2	49.9
ξ_c	4.7e−3 [−]	9.9e−4 [−]

the millimeter range. Assuming that the crack closure pressure P_{cl} is in the order of $E\xi$ (e.g. Guéguen & Sarout 2011), where E is the rock Young modulus and using the values of K_0 and μ_0, and ξ obtained for both samples, we obtain values for P_{cl} of the order of 360 and 75 MPa for L_1 and L_2, respectively. These estimates imply that cracks are likely to be open at the prevailing *in-situ* stress conditions at the GTS (Wenning *et al.* 2018). This aligns with the findings by Möri *et al.* (2021), who argue that that the rock matrix has a connected, water-saturated pore network under *in-situ* stress conditions.

An additional contribution to microcracking could be linked to the alteration of the crystalline rocks during tunnel excavation, referred to as the excavation damage zone (EDZ). At the GTS, the EDZ can extend up to one tunnel diameter (3.5 m) from the tunnel wall (e.g. David *et al.* 2018), with the crack density rapidly decreasing with distance (e.g. Bohlen *et al.* 2007). Such EDZ-related cracks may affect the near-surface seismic measurements. However, measurements based on core samples or sonic log data are expected to be sufficiently distant from the tunnel to be unaffected by the EDZ (e.g. David *et al.* 2018). While potentially persistent EDZ effects cannot be ruled out, drilling-induced cracks may also affect sonic log and core samples measurements (e.g. Li & Richwalski 1996). In this sense, Möri *et al.* (2021) provided evidence of a higher porosity in the immediate vicinity of the borehole wall, with the porosity stabilizing beyond 3 mm into the massive rock where the porosity is dominated by grain-boundary pores.

The widespread presence of microcracks in crystalline settings suggests that frequency-dependent attenuation is likely to be a common feature in underground laboratories. Indeed, frequency-dependent attenuation has also been reported in other crystalline

Table 5. Fitting parameters of *P*-wave attenuation under dry and saturated conditions using eq. (17).

	P-L_1-Dry	P-L_2-Dry	P-L_1-Sat	P-L_2-Sat
Q_i^{-1} (−)	0.027	0.038	0.035	0.046
T ($s^2\,Km^{-2}$)	0.0047	0.0017	0.0042	0.003
D_q (GPa^{-1})	47.5	22.5	6.2	4.6

environments. Notably, in the German KTB (Continental Deep-Drilling Program) site, Li & Richwalski (1996) compared attenuation estimates derived from VSP and sonic log data. The reported values of Q_p of around 30 and 15 at frequencies of around 50 and 15 kHz, respectively, are shown in Fig. 4 (green dots), along with the measurements from GTS. The similarity in the magnitude and frequency dependence of the attenuation between the measurements from KTS and GTS points to the importance of considering microcrack-related WIFF effects when interpreting seismic data acquired in underground laboratories located within crystalline rocks. Particularly due to the fact that crystalline rocks are typically assumed to be perfectly elastic.

5.2 Additional attenuation mechanisms

Meglis *et al.* (1996) demonstrated that the typically observed pressure dependence of *P*-wave attenuation in rocks can be attributed to a combination of crack-related and matrix-related attenuation. Assuming that the total pressure-dependent attenuation of the samples $Q^{-1}(P)$ is the sum of crack-related attenuation Q_c^{-1} and a component of additional inelasticity within the rock Q_i^{-1}, Meglis *et al.* (1996) approximates $Q^{-1}(P)$ as

$$Q^{-1}(P) = Q_c^{-1}(P) + Q_i^{-1} = T V_p^2(P) \exp(-P D_q) + Q_i^{-1}, \quad (17)$$

where the parameters T and D_q as well as Q_i^{-1} are independent of pressure P. As mentioned by Meglis *et al.* (1996), eq. (17) assumes a frictional loss mechanism behind Q_c^{-1}, which depends on an exponentially decreasing crack density as confining pressure increases. Furthermore, the dependence of Q_c^{-1} on pressure is also linked to changes in rock elasticity through the velocity V_P. We fit eq. (17) to our ultrasonic *P*-wave attenuation data to determine the parameters T, D_q and Q_i^{-1}.

As shown in Figs 3(a) and (b), eq. (17) effectively models the behaviour of the observed *P*-wave attenuation under both saturated and dry conditions. The fitting parameters for both samples are given in Table 5. Under dry conditions, the attenuation decay parameter D_q is of the same order as the velocity decay parameter (D in Table 3). Notably, David *et al.* (2018) reported a similar exponential dependence of permeability in the Grimsel granodiorite on effective pressure. Considering effective pressures between 5 and 30 MPa, nine research teams reported values for the stress-sensitivity parameter of the permeability D_κ, which resulted in an average value of $93 \pm 15\ GPa^{-1}$.

Regarding the attenuation contributions, Q_i^{-1} exhibits comparable magnitudes in both dry and saturated scenarios, suggesting that its underlying mechanism is independent of crack presence and saturation. At high confining pressures, where crack-related effects are minimal, possible sources of additional matrix inelasticity within the rock include plastic yielding due to stress concentration around heterogeneities (e.g. Yarushina & Podladchikov 2010). At relatively low confining pressures, where cracks remain open, crack-related mechanisms, such as squirt flow, become relevant. However, other mechanisms may also play a role on $Q_c^{-1}(P)$. Frictional sliding along microcracks surfaces and grain boundaries could partly explain the observed pressure dependence, though its contribution at seismic strains is expected to be limited (e.g. Winkler *et al.* 1979; Mavko *et al.* 2009; Tisato & Quintal 2013; Chapman *et al.* 2023).

We have attempted to avoid mesoscale heterogeneities (e.g. fractures and faults) by selecting intact core samples or regions to limit additional attenuation and dispersion effects. However, some scattering effects due to the presence of microcracks are expected at ultrasonic frequencies (Section 3), which could also explain the observed increase in attenuation at lower pressures. Note that higher confining pressures are required to reach the asymptotic behaviour in dry samples. Since scattering effects are more pronounced for larger compressibility contrasts between cracks and the host rock, dry samples are expected to exhibit stronger scattering. Lastly, we note that the microstructural investigations of the Grimsel granodiorite by Wenning *et al.* (2018) revealed the presence of cm-scale grains, consistent with visual inspections of our samples, which can contribute to scattering independent of the crack population.

Given the scattering effects and other potential contributions, the attenuation values at ultrasonic frequencies likely represent an upper bound for squirt flow attenuation. One could incorporate additional parameters into eq. (5) to account for other contributions such as Q_i^{-1}, to *P*-wave attenuation. Indeed, assuming an additional frequency-independent Q-model, could potentially decrease the slight frequency-dependent attenuation observed within the 50–1200 Hz range, an inconsistency with the anticipated nearly constant behaviour suggested by Holliger & Bühnemann (1996). However, the corresponding modeling of interactions between two or more attenuation mechanisms and their impact on elastic modulus dispersion when fitting a viscoelastic model as in eq. (5), poses significant complexities that are beyond the scope of this study.

6 CONCLUSIONS

We have examined *P*-wave attenuation and velocity measurements representative of the GTS crystalline rocks. The analysis revealed a consistent frequency-dependent behaviour of the seismic attenuation and velocity in the macroscopically intact granodioritic rocks, which can be reproduced by a model of a WIFF mechanism operating at the microscale. Newly acquired pressure-dependent ultrasonic data from intact GTS core samples were found to support the presence of microscale cracks and the physical validity of the WIFF model parameters explaining the observations. By integrating observations from various seismic techniques, we provide evidence of the applicability of WIFF models as well as the magnitude of WIFF effects. This study allowed to advance our understanding of frequency-dependent attenuation and dispersion in macroscopically intact crystalline rocks related to microscopic WIFF effects. This knowledge is essential for the isolation of superimposed attenuation and dispersion effects related to mesoscale fractures, which are prominent targets of seismic studies.

FUNDING

We gratefully acknowledge the financial support of the European Commission through the DISCO2 STORE project, Grant agreement ID: 101007851 of the Horizon 2020 Programme.

ACKNOWLEDGMENTS

JGR gratefully acknowledges the financial support from CONICET (PIP 11220210100346CO). We wish to thank Dr Guo and an anonymous reviewer for the suggestions that helped to improve the quality of the manuscript.

AUTHOR'S CONTRIBUTION

NDB (Conceptualization, Formal analysis, Methodology, Writing—original draft), EAB (Data curation, Methodology), SGS (Formal analysis, Investigation, Methodology, Writing—original draft), JGR (Formal analysis, Methodology, Writing—original draft), EC (Methodology, Resources, Writing—review and editing), KH (Formal analysis, Resources, Writing—review and editing).

DATA AVAILABILITY

The ultrasonic data set and the required files for reproducing the figures presented in this paper are accessible at `http://doi.org/10.5281/zenodo.10510999` (Barbosa 2024).

REFERENCES

Adelinet, M., Fortin, J., Guéguen, Y., Schubnel, A. & Geoffroy, L., 2010. Frequency and fluid effects on elastic properties of basalt: experimental investigations, *Geophys. Res. Lett.,* **37**(2).

Adelinet, M., Fortin, J. & Guéguen, Y., 2011. Dispersion of elastic moduli in a porous-cracked rock: theoretical predictions for squirt-flow, *Tectonophysics,* **503**(1-2), 173–181.

Amann, F. *et al.*, 2018. The seismo-hydromechanical behavior during deep geothermal reservoir stimulations: open questions tackled in a decameter-scale *in situ* stimulation experiment, *Solid Earth,* **9**(1), 115–137.

Anders, M.H., Laubach, S.E. & Scholz, C.H., 2014. Microfractures: A review, *J. Struct. Geol.,* **69,** 377–394.

Barbosa, N.D., 2024. Data for manuscript "Frequency-dependent seismic attenuation and velocity dispersion in crystalline rocks: Insights from the Grimsel Test Site". Barbosa et al. submitted to JGR: Solid Earth. (Version v2), Zenodo.

Barbosa, N.D., Caspari, E., Rubino, J.G., Greenwood, A., Baron, L. & Holliger, K., 2019. Estimation of fracture compliance from attenuation and velocity analysis of full-waveform sonic log data, *J. geophys. Res.: Solid Earth,* **124**(3), 2738–2761.

Barbosa, N.D., Greenwood, A., Caspari, E., Dutler, N. & Holliger, K., 2021. Estimates of individual fracture compliances along boreholes from full-waveform sonic log data, *J. geophys. Res.: Solid Earth,* **126**(5), e2021JB022015.

Bardet, J., 1992. A viscoelastic model for the dynamic behavior of saturated poroelastic soils, *J. Appl. Mech.,* **59,** 128–135.

Batzle, M.L., Han, D.-H. & Hofmann, R., 2006. Fluid mobility and frequency-dependent seismic velocity—direct measurements, *Geophysics,* **71**(1), N1–N9.

Bohlen, T., Lorang, U., Rabbel, W., Müller, C., Giese, R., Lüth, S. & Jetschny, S., 2007. Rayleigh-to-shear wave conversion at the tunnel face—from 3d-fd modeling to ahead-of-drill exploration, *Geophysics,* **72**(6), T67–T79.

Brixel, B., Klepikova, M., Jalali, M.R., Lei, Q., Roques, C., Kriestch, H. & Loew, S., 2020. Tracking fluid flow in shallow crustal fault zones: 1. insights from single-hole permeability estimates, *J. geophys. Res.: Solid Earth,* **125**(4), e2019JB018200.

Carcione, J.M., 2007. *Wave Fields in Real Media: Wave Propagation in Anisotropic, Anelastic, Porous and Electromagnetic Media, Vol. 38,* Elsevier.

Chapman, S., Fortin, J., Gallagher, A. & Borgomano, J.V., 2023. Strain amplitude dependent transition from dynamic to static bulk modulus in rocks with and without pre-existing cracks, *Rock Mech. Rock Eng.,* **56**(8), 6101–6118.

Christensen, N.I. & Mooney, W.D., 1995. Seismic velocity structure and composition of the continental crust: a global view, *J. geophys. Res.: Solid Earth,* **100**(B6), 9761–9788.

Crampin, S. & Gao, Y., 2010. A review of the new understanding of fluid-rock deformation in the crack-critical earth, in *ISRM International Symposium on In-Situ Rock Stress,* pp. ISRM–ISRS, ISRM.

Crampin, S. & Peacock, S., 2005. A review of shear-wave splitting in the compliant crack-critical anisotropic earth, *Wave Motion,* **41**(1), 59–77.

David, C. *et al.*, 2018. Kg^2b, a collaborative benchmarking exercise for estimating the permeability of the Grimsel granodiorite–part 1: measurements, pressure dependence and pore-fluid effects, *Geophys. J. Int.,* **215**(2), 799–824.

de Paula, O.B., Pervukhina, M., Makarynska, D. & Gurevich, B., 2012. Modeling squirt dispersion and attenuation in fluid-saturated rocks using pressure dependency of dry ultrasonic velocities, *Geophysics,* **77**(3), WA157–WA168.

Doetsch, J., Krietsch, H., Schmelzbach, C., Jalali, M., Gischig, V.S., Villiger, L., Amann, F. & Maurer, H., 2020. Characterizing a decametre-scale granitic reservoir using ground-penetrating radar and seismic methods, *Solid Earth,* **11,** 1441–1455.

Dutler, N. *et al.*, 2019. Hydraulic fracture propagation in a heterogeneous stress field in a crystalline rock mass, *Solid Earth,* **10**(6), 1877–1904.

Eulenfeld, T. & Wegler, U., 2016. Measurement of intrinsic and scattering attenuation of shear waves in two sedimentary basins and comparison to crystalline sites in germany, *Geophys. J. Int.,* **205**(2), 744–757.

Green, A. & Mair, J., 1983. Subhorizontal fractures in a granitic pluton; their detection and implications for radioactive waste disposal, *Geophysics,* **48**(11), 1428–1449.

Guéguen, Y. & Sarout, J., 2011. Characteristics of anisotropy and dispersion in cracked medium, *Tectonophysics,* **503**(1-2), 165–172.

Guo, J., Rubino, J.G., Barbosa, N.D., Glubokovskikh, S. & Gurevich, B., 2017. Seismic dispersion and attenuation in saturated porous rocks with aligned fractures of finite thickness: theory and numerical simulations—Part I: *P*-wave perpendicular to the fracture plane, *Geophysics,* **83**(1), WA49–WA62.

Gurevich, B. & Pevzner, R., 2015. How frequency dependency of *Q* affects spectral ratio estimates, *Geophysics,* **80**(2), A39–A44.

Gurevich, B., Brajanovski, M., Galvin, R.J., Müller, T.M. & Toms-Stewart, J., 2009. *P*-wave dispersion and attenuation in fractured and porous reservoirs–poroelasticity approach, *Geophys. Prospect.,* **57**(2), 225–237.

Gurevich, B., Makarynska, D., de Paula, O.B. & Pervukhina, M., 2010. A simple model for squirt-flow dispersion and attenuation in fluid-saturated granular rocks, *Geophysics,* **75**(6), N109–N120.

Holliger, K. & Bühnemann, J., 1996. Attenuation of broad-band (50–1500 Hz) seismic waves in granitic rocks near the earth's surface, *Geophys. Res. Lett.,* **23**(15), 1981–1984.

Hunziker, J., Greenwood, A., Minato, S., Barbosa, N.D., Caspari, E. & Holliger, K., 2020. Bayesian full-waveform inversion of tube waves to estimate fracture aperture and compliance, *Solid Earth,* **11**(2).

Johnson, D.L., Koplik, J. & Dashen, R., 1987. Theory of dynamic permeability and tortuosity in fluid-saturated porous media, *J. Fluid Mech.,* **176,** 379–402.

Kachanov, M., 1992. Effective elastic properties of cracked solids: critical review of some basic concepts, *ASME. Appl. Mech. Rev.,* **45,** 304–335 .

Krietsch, H., Gischig, V., Evans, K., Doetsch, J., Dutler, N.O., Valley, B. & Amann, F., 2019. Stress measurements for an *in situ* stimulation experiment in crystalline rock: integration of induced seismicity, stress relief and hydraulic methods, *Rock Mech. Rock Eng.,* **52,** 517–542. doi:

Krietsch, H. *et al.*, 2020. Hydromechanical processes and their influence on the stimulation effected volume: observations from a decameter-scale hydraulic stimulation project, *Solid Earth,* **11**(5), 1699–1729.

Li, X.-P. & Richwalski, S., 1996. Seismic attenuation and velocities of p-and s-waves in the german ktb area, *J. Appl. Geophys.,* **36**(2-3), 67–76.

Li, Y., David, E.C., Nakagawa, S., Kneafsey, T.J., Schmitt, D.R. & Jackson, I., 2018. A broadband laboratory study of the seismic properties of cracked and fluid-saturated synthetic glass media, *J. geophys. Res.: Solid Earth,* **123**(5), 3501–3538.

Lüth, S., Giese, R., Otto, P., Krüger, K., Mielitz, S., Bohlen, T. & Dickmann, T., 2008. Seismic investigations of the piora basin using s-wave conversions at the tunnel face of the piora adit (gotthard base tunnel), *Int. J. Rock Mech. Min. Sci.,* **45**(1), 86–93.

Majer, E.L., Myer, L., Peterson, J., Karasaki, K., Long, J., Martel, S., Blumling, P. & Vomvoris, S., 1990. Joint seismic, hydrogeological, and geomechanical investigations of a fracture zone in the Grimsel Rock Laboratory, Switzerland, Tech. rep., Lawrence Berkeley Lab., CA (USA); Nationale Genossenschaft fuer die Lagerung Radioaktiver Abfaelle (NAGRA), Baden (Switzerland).

Marelli, S., 2011. Seismic imaging of temporal changes in underground radioactive waste repositories: surveillance requirements and full waveform inversion issues, Ph.D. thesis, ETH Zurich.

Mavko, G., Mukerji, T. & Dvorkin, J., 2009. *The Rock Physics Handbook: Tools for Seismic Analysis of Porous Media,* Cambridge Univ. Press.

Meglis, I., Greenfield, R., Engelder, T. & Graham, E., 1996. Pressure dependence of velocity and attenuation and its relationship to crack closure in crystalline rocks, *J. geophys. Res.: Solid Earth,* **101**(B8), 17 523–17 533.

Molyneux, J.B. & Schmitt, D.R., 2000. Compressional-wave velocities in attenuating media: a laboratory physical model study, *Geophysics,* **65**(4), 1162–1167.

Möri, A., Mazurek, M., Ota, K., Siitari-Kauppi, M., Eichinger, F. & Leuenberger, M., 2021. Quantifying the porosity of crystalline rocks by *in situ* and laboratory injection methods, *Minerals,* **11**(10), 1072.

Müller, T.M., Gurevich, B. & Lebedev, M., 2010. Seismic wave attenuation and dispersion resulting from wave-induced flow in porous rocks—a review, *Geophysics,* **75**(5), 75A147–75A164.

Nasseri, M., Schubnel, A., Benson, P. & Young, R., 2009. Common evolution of mechanical and transport properties in thermally cracked westerly granite at elevated hydrostatic pressure, *Pure appl. Geophys.,* **166,** 927–948.

Obermann, A., Kraft, T., Larose, E. & Wiemer, S., 2015. Potential of ambient seismic noise techniques to monitor the st. gallen geothermal site (switzerland), *J. geophys. Res.: Solid Earth,* **120**(6), 4301–4316.

Ògúnsànmí, A. *et al.*, 2021. Elastic properties of a reservoir sandstone: a broadband inter-laboratory benchmarking exercise, *Geophys. Prospect.,* **69**(2), 404–418.

Pandey, S., Vishal, V. & Chaudhuri, A., 2018. Geothermal reservoir modeling in a coupled thermo-hydro-mechanical-chemical approach: A review, *Earth-Sci. Rev.,* **185,** 1157–1169.

Picotti, S. & Carcione, J.M., 2006. Estimating seismic attenuation (q) in the presence of random noise, *J. Seism. Exp.,* **15**(2), 165–181.

Pimienta, L., Orellana, L. & Violay, M., 2019. Variations in elastic and electrical properties of crustal rocks with varying degree of microfracturation, *J. geophys. Res.: Solid Earth,* **124**(7), 6376–6396.

Pride, S.R., Berryman, J.G. & Harris, J.M., 2004. Seismic attenuation due to wave-induced flow, *J. geophys. Res.: Solid Earth,* **109**(B1).

Quan, Y. & Harris, J.M., 1997. Seismic attenuation tomography using the frequency shift method, *Geophysics,* **62**(3), 895–905.

Quiroga, G.E., Rubino, J.G., Solazzi, S.G., Barbosa, N.D., Favino, M. & Holliger, K., 2023. Seismic signatures of partial steam saturation in fractured geothermal reservoirs: Insights from poroelasticity, *Geophysics,* **88**(5), WB89–WB104.

Rørheim, S., 2022. On frequency-dependent rock experiments: A comparative review, arXiv preprint arXiv:2208.03795.

Rubino, J.G., Barbosa, N.D., Hunziker, J. & Holliger, K., 2022. Can we use seismic reflection data to infer the interconnectivity of fracture networks?, *Geophys. J. Int.,* **231**(2), 996–1010.

Rutqvist, J. & Stephansson, O., 2003. The role of hydromechanical coupling in fractured rock engineering, *Hydrol. J.,* **11**(1), 7–40.

Sams, M., Neep, J., Worthington, M. & King, M., 1997. The measurement of velocity dispersion and frequency-dependent intrinsic attenuation in sedimentary rocks, *Geophysics,* **62**(5), 1456–1464.

Sarout, J., 2012. Impact of pore space topology on permeability, cut-off frequencies and validity of wave propagation theories, *Geophys. J. Int.,* **189**(1), 481–492.

Shapiro, S.A., 2003. Elastic piezosensitivity of porous and fractured rocks, *Geophysics,* **68**(2), 482–486.

Sotelo, E., Rubino, J.G., Solazzi, S.G., Barbosa, N.D. & Holliger, K., 2021. Fractures in low-permeability rocks: Can poroelastic effects associated with damage zones enhance their seismic visibility?, *J. geophys. Res.: Solid Earth,* **126**(5), e2020JB021155.

Subramaniyan, S., Quintal, B., Tisato, N., Saenger, E.H. & Madonna, C., 2014. An overview of laboratory apparatuses to measure seismic attenuation in reservoir rocks, *Geophys. Prospect.,* **62**(6), 1211–1223.

Sun, Y. & Gurevich, B., 2020. Modeling the effect of pressure on the moduli dispersion in fluid-saturated rocks, *J. geophys. Res.: Solid Earth,* **125**(8), e2019JB019297.

Tarif, P. & Bourbie, T., 1987. Experimental comparison between spectral ratio and rise time techniques for attenuation measurement, *Geophys. Prospect.,* **35**(6), 668–680.

Thomsen, L., 1986. Weak elastic anisotropy, *Geophysics,* **51**(10), 1954–1966.

Tisato, N. & Quintal, B., 2013. Measurements of seismic attenuation and transient fluid pressure in partially saturated berea sandstone: evidence of fluid flow on the mesoscopic scale, *Geophys. J. Int.,* **195**(1), 342–351.

Wenning, Q.C., Madonna, C., de Haller, A. & Burg, J.-P., 2018. Permeability and seismic velocity anisotropy across a ductile-brittle fault zone in crystalline rock, *Solid Earth,* **9,** 683–698.

Winkler, K. & Nur, A., 1979. Pore fluids and seismic attenuation in rocks, *Geophys. Res. Lett.,* **6**(1), 1–4.

Winkler, K., Nur, A. & Gladwin, M., 1979. Friction and seismic attenuation in rocks, *Nature,* **277**(5697), 528–531.

Yarushina, V.M. & Podladchikov, Y.Y., 2010. Plastic yielding as a frequency and amplitude independent mechanism of seismic wave attenuation, *Geophysics,* **75**(3), N51–N63.

Zangerl, C., Eberhardt, E. & Loew, S., 2003. Ground settlements above tunnels in fractured crystalline rock: numerical analysis of coupled hydromechanical mechanisms, *Hydrogeol. J.,* **11,** 162–173.

APPENDIX A: ADDITIONAL DETAILS REGARDING LEGACY DATA

In this appendix, we summarize the key seismic attributes and computed values derived from the reviewed studies in Section 2.

A1 Near-surface survey of Holliger and Bühnemann (1996)

Various types of seismic sources were placed in water-filled boreholes and along the tunnel wall. Geophones were anchored in small holes drilled for this purpose along the tunnel wall. Reported Q_P-values correspond to those estimated using explosive charges as the associated signals exhibited the broadest (∼50–1500 Hz) and most uniform frequency spectrum as well as the best signal-to-noise ratio.

The Q_P-estimates were derived from the first cycles of transmitted P-waves using the spectral ratio method (e.g. Tarif & Bourbie 1987) and assuming that both the velocity and Q_P remained frequency-independent within the prevailing spectral range. The authors also noted that the linear correlation coefficients for the

Q_P-estimates were around 0.8, indicating a negligible frequency dependence of Q_P within the considered range (i.e. 50–1200 Hz). Following this assumption, Q_P was estimated by analysing the slope of the frequency-dependent ratio of the amplitude spectra recorded at two distinct locations. The Q_P-estimates ranged from 20 to 60, with a median of 35 and standard errors below 20 per cent. The thus inferred values were considered representative of the granodioritic host rock at GTS.

To account for potential variability in V_P, we consider an uncertainty of 100 m s^{-1}, which is consistent with a value derived from comparable works conducted at the GTS (Doetsch *et al.* 2020). The associated uncertainty in frequency is 575 Hz, implying that the reported values are expected to be representative across the range from 50 to 1200 Hz used to estimate Q_P. The values extracted from Holliger & Bühnemann (1996) are presented in Table 1.

A2 Near-surface survey of Doetsch et al. (2020)

The principal aim of the study by Doetsch *et al.* (2020) was to image the main geological structures relevant to the ISC project using seismic travel-time tomography. This study involved both tunnel-to-tunnel and 3-D-type configurations.

For the tunnel-to-tunnel configuration, a total of 120 geophones were strategically placed along the walls of the VE-tunnel (Fig. 1) at 0.5-m intervals. Seismic signals were generated using a small hammer and chisel, with 120 source points evenly spaced at intervals of 0.5 m along the AU tunnel (Fig. 1). This setup resulted in the acquisition of 9500 high-quality first-arrival travel times. The estimated picking uncertainty was 0.04 ms.

For the 3-D tomography, 26 piezoelectric receivers were installed for passive and active seismic monitoring. A sparker source was activated within six water-filled boreholes associated with the ISC project (the two INJ boreholes shown in Fig. 1 and four additional GEO boreholes), generating a data set consisting of 448 source positions, each spaced at regular 0.5 m intervals. Additional hammer strokes along the AU and VE tunnels served as complementary sources. In total, 10,050 first-arrival travel times were picked, with an estimated uncertainty of 0.02 ms.

Due to the foliation of the Grimsel granodiorite, the seismic velocities exhibit anisotropy (e.g. Wenning *et al.* 2018). The authors assume a transversely isotropic medium to model velocity anisotropy using:

$$V_P = v_0(1 + \delta \sin^2(\theta)\cos^2(\theta) + \epsilon \sin^4(\theta)), \quad \text{(A1)}$$

where v_0 is the velocity in the direction normal to the anisotropy plane, θ is the angle between the wave propagation direction and the symmetry axis and ϵ and δ correspond to the classic Thomsen (1986) anisotropy parameters. The anisotropic symmetry axis was assumed to be known during inversion. Using the 3-D tomography data, Doetsch *et al.* (2020) inferred values for ϵ and δ equal to 0.065 and 0.038, respectively, which were consistent with the tunnel-to-tunnel results.

For v_0, they obtained a distribution of values due to the inhomogeneity of the rock within the probed volume. In particular, they provided v_0-values for boreholes INJ1 and INJ2. For the less fractured shallow sections, which are more representative of the granodioritic host rock, v_0-values ranged from 4950 to 5150 m s^{-1}.

To estimate representative values of the seismic attributes and survey frequency, we assume $v_0 = 5050$ m s^{-1} and apply eq. (A1) to compute a mean velocity value for a range of incidence angles from 0° to 180°. The uncertainty is obtained from the mean value when considering $v_0 = 4950$ m s^{-1}, which would be the same for $v_0 = 5150$ m s^{-1}. As a result, we obtain a mean velocity $\bar{V}_P$ of 5200 m s^{-1} and an uncertainty ΔV_P of approximately 100 m s^{-1}.

While a mean frequency $\bar{f}_{\text{surv}}$ of 1.1 kHz was reported, the associated variability is unknown. We consider the work of Marelli (2011) on the use of sparker sources at the GTS, which showed that signals can have significant energy up to ∼3 kHz and high spectral amplitudes in the range from 500 to 1500 Hz. We thus assume an uncertainty Δf_{surv} of 0.5 kHz. Finally, Q_P-values were not reported by Doetsch *et al.* (2020). The values extracted from Doetsch *et al.* (2020) are presented in Table 1.

A3 Near-surface survey of Majer et al. (1990)

In the context of the Fracture Research Investigation (FRI) project at the GTS, Majer *et al.* (1990) conducted a series of multi-offset/multi-source vertical seismic profiling (VSP) experiments to characterize the seismic response of fractures within their study area. The FRI site was situated in the southern part of the GTS, near the boundary between the Grimsel granodiorite and the so-called Central Aaregranite.

The authors employed borehole seismic methods, specifically VSP and cross-hole surveys, using data acquired from boreholes BOFR 87.001 and BOFR 87.002, which extended from the AU tunnel to the access tunnel. These boreholes allowed for cross-hole seismic studies, core sampling of the fracture zone and hydraulic testing. Additionally, a series of 76 shallow holes (74 mm in diameter, 50 cm deep) were drilled into the tunnel walls at 0.25 m intervals, allowing for the placement of seismic sources and receivers. Seismic sources were positioned in both the boreholes and shallow holes, and the data were recorded using three-component accelerometers spaced at 0.5 m intervals.

Using this experimental setup, three seismic surveys were conducted, with particular focus given to the 1987 and 1988 experiments, as they were performed under ambient saturation conditions. The collected seismograms spanned nearly 60 000 ray paths across the FRI zone, with source–receiver distances ranging from 0.5 to 23 m. The peak energy transmission in these surveys occurred at frequencies between 5 and 10 kHz.

For their tomographic analysis, Majer *et al.* (1990) performed manual traveltime picking from the radial component of the recorded data, aligning with the strongest *P*-wave motion. They noted that the 1988 data set showed less scattering than the 1987 data set, likely due to an increase in water saturation following hydraulic experiments conducted shortly before the 1988 survey. This saturation increase could explain the consistently higher seismic velocities observed in 1988 relative to 1987. Given its superior data quality, the authors relied primarily on the 1988 data set for attenuation analysis.

To account for the known anisotropy of the crystalline rock at the GTS, the authors performed a tomographic inversion using the velocity model

$$V_P^2 = A + B\sin(2\theta) + C\cos(2\theta) + D\sin(4\theta) + E\cos(4\theta), \quad \text{(A2)}$$

where θ represents the wave propagation direction. The anisotropy parameters obtained from fitting this model to the 1987 and 1988 data sets were:

- 1987: $A = 26.211$ km^2 s^{-2}, $B = 0.544$ km^2 s^{-2}, $C = -1.122$ km^2 s^{-2}, $D = -0.331$ km^2 s^{-2}, $E = -0.185$ km^2 s^{-2}
- 1988: $A = 27.942$ km^2 s^{-2}, $B = 1.375$ km^2 s^{-2}, $C = -0.633$ km^2 s^{-2}, $D = -0.309$ km^2 s^{-2}, $E = -0.196$ km^2 s^{-2}

Using these parameters, we computed mean velocity values by averaging over the range $\theta = 0^\circ$ to 180°. The final mean velocity and its associated uncertainty were determined as the midpoint and standard deviation between the 1987 and 1988 results, yielding an average velocity of approximately 5200 m s^{-1}. This value aligns well with previous studies, such as Doetsch *et al.* (2020). Additionally, an alternative inversion approach considering only cross-hole travel times yielded a similar mean velocity of 5260 m s^{-1} for the 1988 survey.

For attenuation estimation, Majer *et al.* (1990) applied an inversion procedure to the first arrival amplitudes, assuming that the recorded amplitudes were representative of the initial energy received. This analysis included corrections for geometric spreading and source radiation pattern effects. The geometric spreading correction involved multiplying the measured amplitudes by the travel distance, while the source radiation pattern was modeled as a dipole-type cosine function.

The attenuation coefficient, α, was estimated by averaging values from the five largest amplitudes in the data set, yielding a representative value of 0.3 m^{-1}. From this coefficient, the authors computed the *P*-wave quality factor, Q_P, using the relation:

$$Q_P = \frac{\pi f_{\text{surv}}}{\alpha V_P}. \tag{A3}$$

Taking $\bar{f}_{\text{surv}} = 7500$ Hz and the mean velocity values for the 1987 and 1988 surveys, we obtained a mean and standard deviation for Q_P of 15.1 and 2.9, respectively. The corresponding inverse quality factor values, Q_P^{-1}, are presented in Table 1.

A4 FWS results of Barbosa et al. (2019)

Barbosa *et al.* (2019) analysed FWS log data along borehole INJ2, which is approximately 45 m deep with a nominal diameter of 146 mm. The borehole intersects multiple fractures within the granodioritic rock mass. The FWS tool used a monopole source positioned 91.4 cm (3 feet) from an array of three receivers spaced at 30.48 cm (1-foot) intervals. Multiple static measurements were taken at each depth, with approximately 50 traces being stacked to improve the signal-to-noise ratio.

The sonic *P*-wave phase velocity profile was determined for both intact and fractured borehole sections. Phase velocities were computed by comparing phase spectra between two receivers, using the amplitude spectrum peak at the receiver closest to the source as a reference. Given the close nominal frequencies (15 and 25 kHz), velocity measurements at both frequencies primarily ensured reliability rather than quantifying velocity dispersion effects. Both frequency sets were used to estimate a mean value for V_P and f_{surv}, with associated uncertainty.

For attenuation analysis, the spectral ratio method was used to separate geometric spreading, fracture-related scattering, and intrinsic attenuation. Numerical simulations and FWS data from different source-receiver offsets provided consistent geometric spreading corrections. Intrinsic attenuation was extracted from intact borehole sections identified via televiewer images, yielding Q_P-values between 12 and 14.5. Barbosa *et al.* (2019) categorized measurements into three borehole sections (upper, central, lower), with the upper section being the least fractured. We consider their upper section results to characterize the Grimsel granodiorite, as it exhibits minimal depth-dependent variations in velocity and attenuation. The extracted values are summarized in Table 1.

A5 Ultrasonic measurements of Majer et al. (1990)

Majer *et al.* (1990) performed ultrasonic experiments on intact and fractured specimens extracted from borehole BOFR 87.003. Here, we focus on their results for an intact specimen measuring 130 mm in length and 116 mm in diameter. The transducers used in these tests operated at distinct frequency ranges, with their frequency characteristics determined via experiments on aluminum calibration samples. Peak spectral amplitudes were observed at approximately 475 and 900 kHz for *P* waves, corresponding to the low- and high-frequency transducers, respectively.

Velocity and amplitude measurements were conducted under varying axial stress conditions, both in dry and water-saturated states. Our analysis considers only the results under saturated conditions at stress levels comparable to the GTS *in-situ* field. Velocities were derived from the initial waveform arrivals, showing an increase with axial stress, consistent with progressive crack closure. The digitized velocity data from Majer *et al.* (1990) were extracted from figs 3.16 and 3.18 of their study for both transducer sets. A mean *P*-wave velocity value and standard deviation were computed for axial stresses ranging from 80 to 150 kN, with unit conversions based on Majer *et al.* (1990) (1 kN = 0.095 MPa).

Since the exact representative frequency for the rock experiments was not reported, we assumed $\bar{f}_{\text{surv}}$ values similar to those obtained for aluminum samples (475 kHz and 900 kHz), though these likely represent an upper bound. For uncertainty estimation, we adopted an approximate 10 per cent variation in $\bar{f}_{\text{surv}}$, based on similar ultrasonic experiments described in Section 2.7. Although Majer *et al.* (1990) qualitatively assessed amplitude decay using peak-to-peak amplitudes, they did not provide direct Q_P-values. The extracted velocity values for low- and high-frequency measurements are reported in Table 1 as 'LF-ultrasonic' and 'HF-ultrasonic', respectively.

APPENDIX B: ULTRASONIC DATA ANALYSIS

B1 Data analysis

We measured *P*- and *S*- wave arrivals using the pulse transmission technique. The measurements were conducted up to ∼50 MPa confining pressure at room temperature conditions. During ultrasonic acquisition, pore pressure was kept constant and equal to room pressure. The measurements were taken on two plugs extracted from a core of borehole INJ1 at GTS (Fig. 1). The rock sample as well as the equipment employed for the ultrasonic measurements are illustrated in Fig. B1. We consider samples with two different lengths, $L_1 = 5.87$ cm and $L_2 = 7.34$ cm. The resonance frequency of the transducers was set to 1 MHz. The source signal for *P*- and *S*-wave transducers was obtained by averaging 7 endcap-to-endcap signals obtained for confining pressures between 25 and 35 MPa (Fig. B2).

Measurements on samples were recorded across the pressure range of ∼0 to ∼50 MPa to investigate the properties closest to present-day low-pressure conditions at the GTS [minimum principal stress 8 to 12 MPa and maximum principal stress 13 to 17 MPa following Wenning *et al.* (2018)]. The seismic waveforms as a function of confining pressures and saturation condition (i.e. dry and water-saturated) for *P*- and *S*-wave transducers are shown in Figs B3 and B4, respectively.

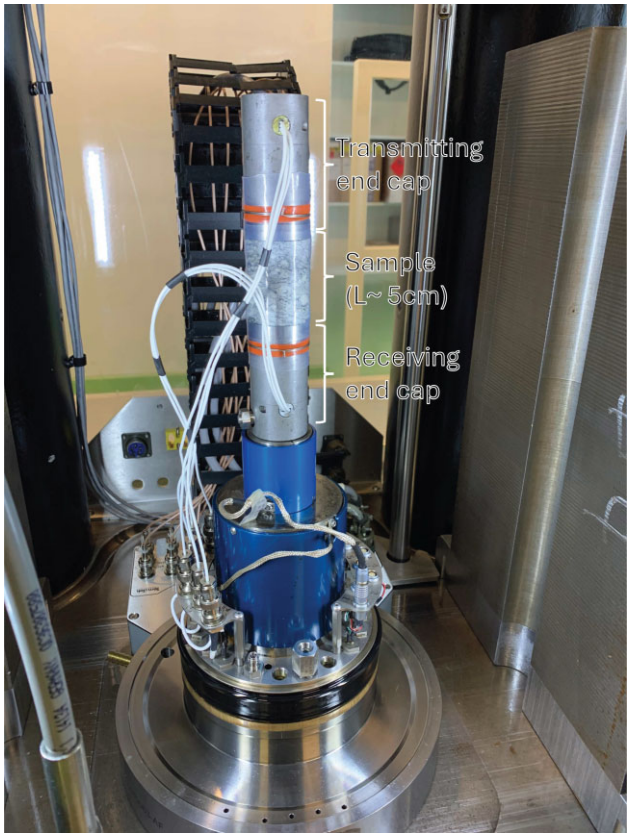

Figure B1. A typical stack for ultrasonic measurements under confining pressure. The core axes are oblique to the foliation. The samples are mounted on ultrasonic velocity endcaps (EC) made of titanium, which are designed to operate in a triaxial test pressure vessel capable of reaching high confining pressures. The plugs were subjected to hydrostatic pressure. Ultrasonic measurements were acquired after the desired confining pressure was reached.

To compute seismic wave velocities and attenuation as a function of confining pressure, we extracted the *P*- and *S*-wave arrivals from the rest of the arrivals (Figs B5 and B6, respectively). For time windowing, we employed a cosine function (e.g. Barbosa *et al.* 2019). Due to the low-quality of the recordings for *S*-wave transducers under saturated conditions (Figs B4 a and b), we have not taken them into account for the remaining of the analysis.

Note that attenuation and velocity estimation is influenced by multiple factors, including signal quality, rock heterogeneity, stress and saturation state as well as the particular method and parameters used for the spectral analysis. To assess the robustness of our velocity and attenuation estimates, we considered the effect of varying the time window used to isolate the arrivals. We compared results obtained using one- and two-cycle windows of the *P*- and *S*-wave modes. While the use of a longer time window is expected to be affected by later arrivals, the overall trends with pressure remained consistent. The variability in *P*-wave velocity was generally below 5 per cent, while attenuation estimates varied by up to 20 per cent. These differences are comparable to those observed when analysing the two independently tested specimens (Figs 2 and 3). The uncertainties reported in Table 1 mainly reflect the variability arising from the limited knowledge of the exact *in-situ* stress conditions, requiring us to consider a plausible range of stress values around a reference.

Finally, as we performed the attenuation and velocity analysis in the frequency domain, we also show the amplitude spectra of the extracted arrivals as functions of frequency and confining pressure (Figs B7 and B8). It is interesting to note that the peak frequency of the amplitude spectra (red circles in Figs B7 and B8) exhibits a clear pressure dependence. This characteristic indicates that a crack-related mechanism may produce a frequency-dependent behaviour of seismic waves, as cracks aspect ratios are modified by a confining pressure increase.

B2 Velocity and attenuation estimates

B2.1 Group velocities

We computed group delay times for *P*- and *S*-wave arrivals as (e.g. Molyneux & Schmitt 2000)

$$\Delta t_g(\omega) = \frac{d(\Delta\Phi(\omega))}{d\omega}, \tag{B1}$$

where $\Delta\Phi$ denotes the difference of the phase spectra of the endcap-to-endcap (EC) signal (Fig. B2) and the signal obtained after transmission through the sample after applying time-windowing (Figs B5 and B6). For the time windowing of EC signal, we centre a cosine function around the picking time illustrated with a red star in Fig. B2. We picked the same minima for the EC and sample signals to make the group time delays comparable to the picking delays. We have verified that group, phase, and picking time delays provided similar magnitudes and pressure dependences.

The group velocities were obtained as $L/\Delta t_g(\omega_{\max})$, where L denotes the sample length and the time delay is computed at the peak of the amplitude spectrum $\omega_{\max}$ of the signal propagating through the sample (red circles in Figs B7 and B8 show the values of $f_{\max} = \omega_{\max}/2\pi$). The resulting group *P*- and *S*-wave velocities as functions of (i) confining pressure, (ii) saturation condition, and (iii) sample length are shown in Fig. 2 of the main body of this work.

B2.2 Attenuation

To estimate attenuation, we use the frequency shift method proposed by Quan & Harris (1997). We first define the spectral centroid and variance using the amplitude spectra of the transmitted signals across the samples (Figs B7 and B8) as well as of the EC signal. The centroid frequency f_s and variance σ_s^2 of the signal $S(f)$ are defined as (Quan & Harris 1997)

$$f_s = \frac{\int_0^\infty f S(f)\mathrm{d}f}{\int_0^\infty S(f)\mathrm{d}f},$$
$$\sigma_s^2 = \frac{\int_0^\infty (f-f_s)^2 S(f)\mathrm{d}f}{\int_0^\infty S(f)\mathrm{d}f}. \tag{B2}$$

We have approximated the integrals in eq. (B2) with summations from 0 to $f_{\mathrm{up}} = kf_{\max}$ to cover the most meaningful amplitudes of the spectra relative to their maxima. For a Gaussian amplitude spectrum, f_s coincides with $f_{\max}$. Given that the amplitude spectra of the signal is approximately Gaussian in most cases (Fig. B9), we have determined the factor k that minimizes the difference between f_s and $f_{\max}$ for the EC amplitude spectrum. Following this procedure, we get $k = 1.82$, which is similar to the typically considered cut-off frequency (e.g. Picotti & Carcione (2006) use $k = 2$). Fig. B9 shows the EC amplitude spectra, the value of f_s (black cross), and the limit of summation f_{up} (black dashed line). For illustration purposes, we also show the amplitude spectra for the *P*-wave signal received for sample L_1 under saturated conditions and for confining pressures

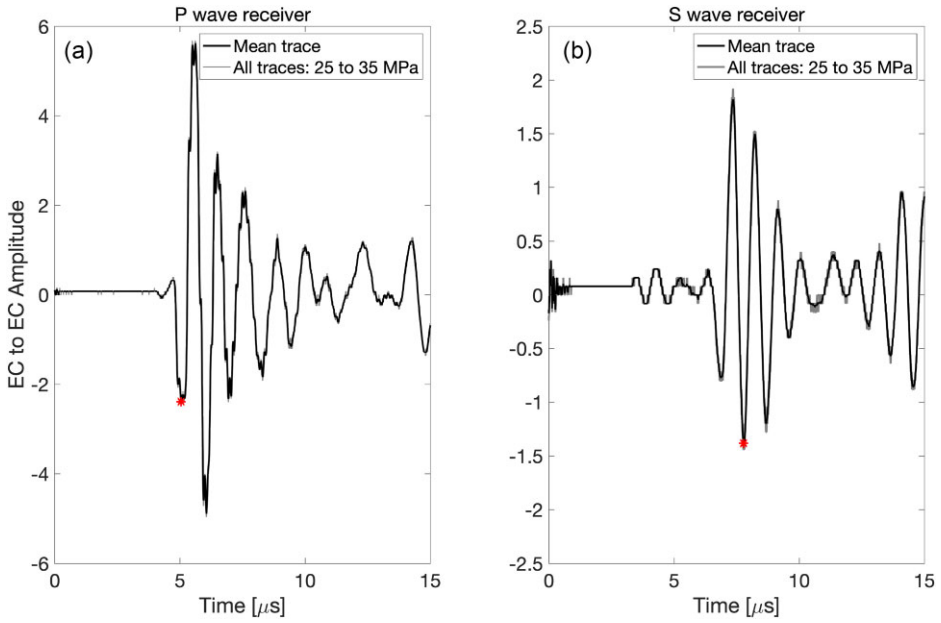

Figure B2. Source signal waveforms. We consider 7 endcap-to-endcap traces (grey solid lines), which were obtained for confining pressures ranging from ∼25 to ∼35 MPa. The signals are highly repeatable, are sampled at 0.01 μs intervals and have length of 2500 samples. We used both (a) *P*- and (b) *S*-wave transducers and computed the mean trace (black solid line) to obtain a reference source signal. The red stars indicate the waveform cycle used for computing picking velocities as well as the centre considered for time-windowing.

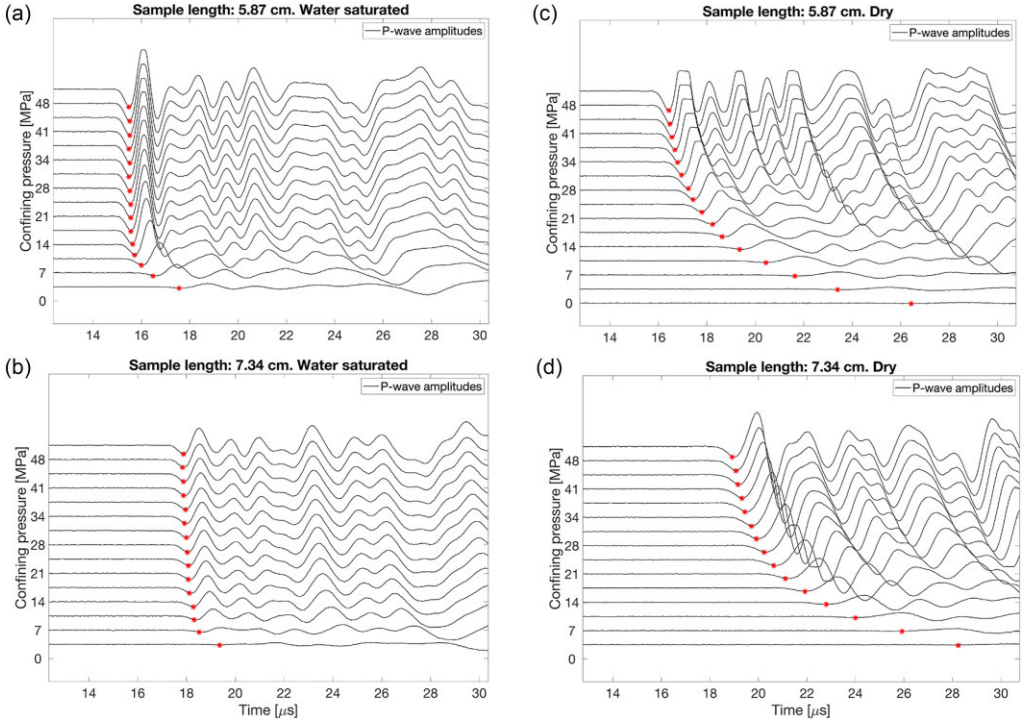

Figure B3. Seismic waveforms as a function of confining pressure for the *P*-wave transducers. Waveforms recorded during *P*-wave transmission experiments at stepwise decreases in pressure (unloading cycle) under (a,b) saturated and (c,d) dry conditions and for samples (a,c) L_1 and (b,d) L_2. The measurements were made at room temperature. Low-quality recordings were removed from the data set (e.g. signals recorded at ∼0 MPa in panels a, b and d).

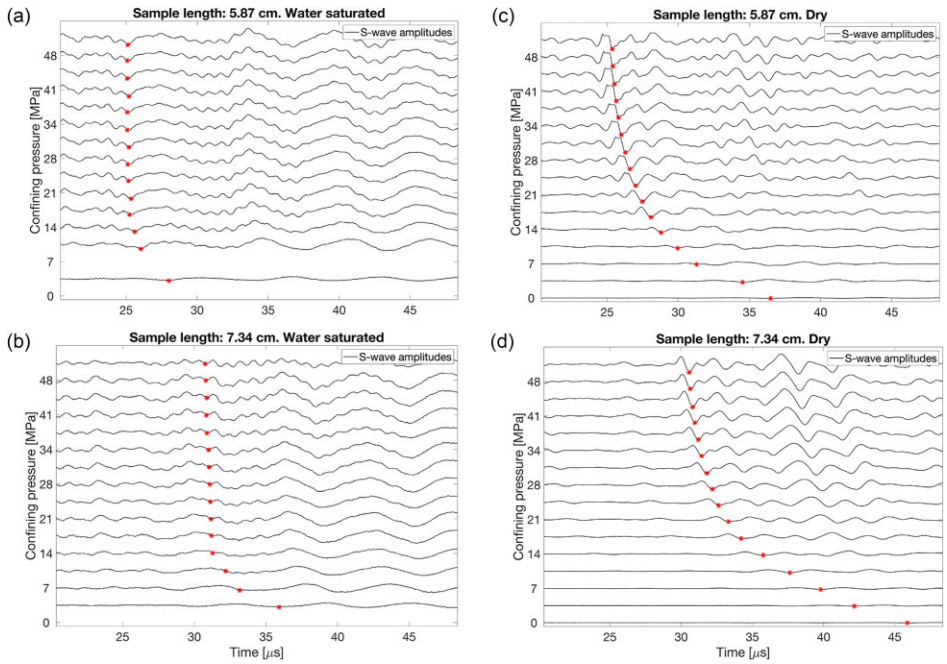

Figure B4. Seismic waveforms as a function of confining pressure for the *S*-wave transducers. Waveforms recorded during *S*-wave transmission experiments at stepwise decreases in pressure (unloading cycle) under (a,b) saturated and (c,d) dry conditions and for samples (a,c) L_1 and (b,d) L_2. The measurements were made at room temperature. Based on the observed poor quality of the recorded waveforms under saturated conditions, only data for dry samples (c, d) was considered. Low-quality recordings were removed from the data set (e.g. signal at ∼7 MPa in panel a).

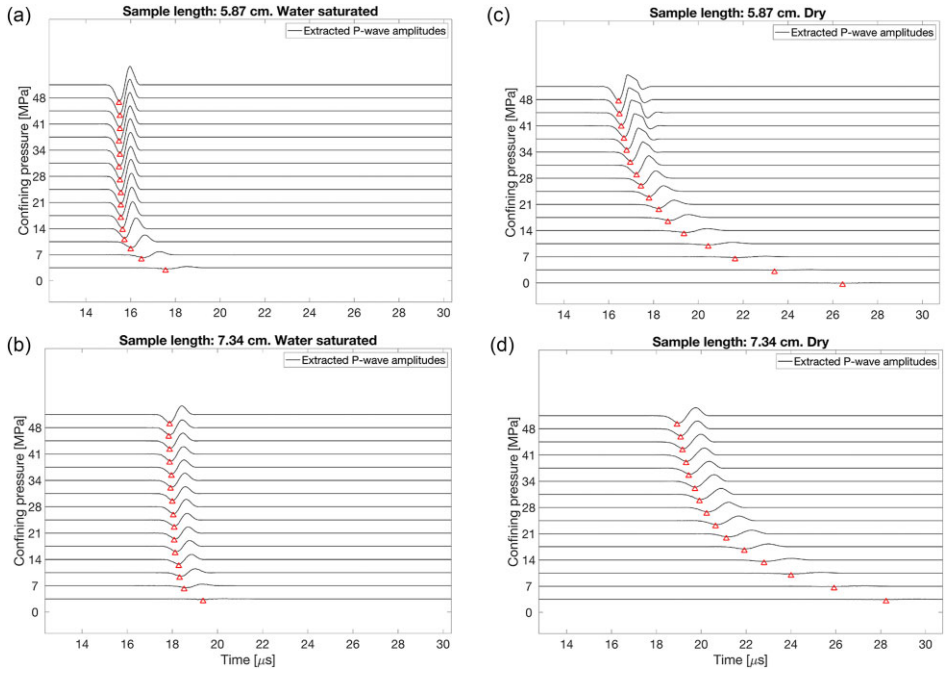

Figure B5. Extracted *P*-waveforms as a function of confining pressure. First *P*-wave arrival under (a,b) saturated and (c,d) dry conditions. The signals were extracted from the arrivals shown in Figs B3 using a time window whose centre is denoted by the red triangles. The window length was chosen to minimize the zero-frequency component of the amplitude spectrum of the extracted signal.

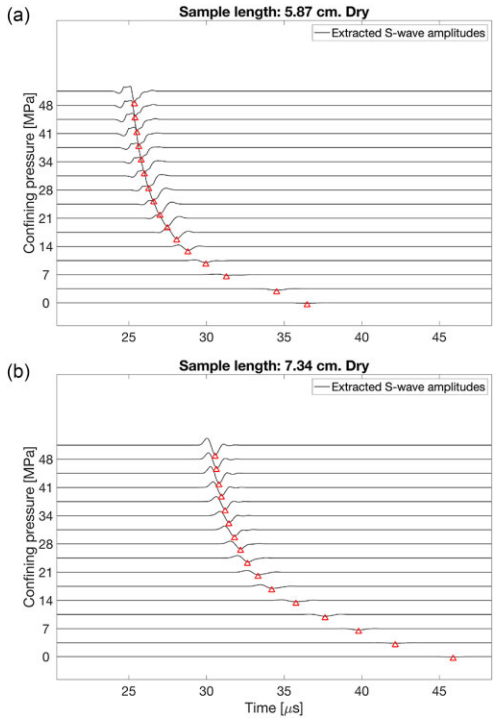

Figure B6. Extracted *S*-waveforms as a function of confining pressure. *S*-wave arrival under dry conditions for sample lengths of (a) 5.87 cm and (b) 7.34 cm. The signals were extracted from the arrivals shown in Fig. B4 c and d using a time window whose centre is denoted by the red triangles. The window length was chosen to minimize the zero-frequency component of the amplitude spectrum of the extracted signal.

representative of the GTS *in-situ* stress field (∼8 to ∼17 MPa). We observe that using the factor k to define the limit of the summation allows us to get a value of f_s that is very close to $f_{\max}$ in all cases (coloured curves in Fig. B9). Although amplitudes in Fig. B9 are normalized we can still observe a key indicator of intrinsic attenuation: a shift in f_s in the sample response with respect to the one associated with the source signal. Furthermore, note that the clear trend of increasing f_s with increasing confining pressures is consistent with a crack-related intrinsic attenuation mechanism as cracks present in the sample are expected to close with increasing confining pressures.

Finally, the attenuation was computed as

$$Q^{-1}(\omega_{\max}) = \frac{f_s^{EC} - f_s^{R}}{\pi(\sigma_s^{EC})^2 \Delta t_g(\omega_{\max})}, \tag{B3}$$

with the superscripts EC and R denoting the EC and receiver signal (sample response), respectively. As for the velocities, *P*- and *S*-wave attenuation values obtained using eqs (B2) to (B3) as functions of confining pressure, saturation condition and sample length are shown in the main body of this work (Fig. 3).

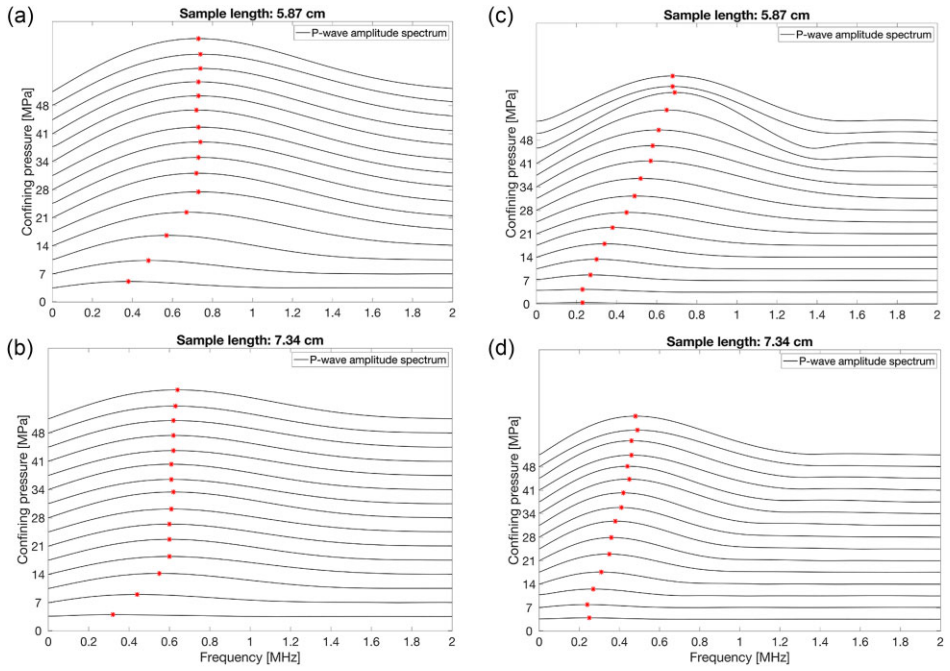

Figure B7. Amplitude spectra of extracted *P*-waveforms as a function of confining pressure. Amplitude spectra obtained by applying Fourier transform to the first *P*-wave arrivals (Fig. B5) under (a,b) saturated and (c,d) dry conditions. Red circles denote the peak frequency of the spectrum to highlight its pressure dependence.

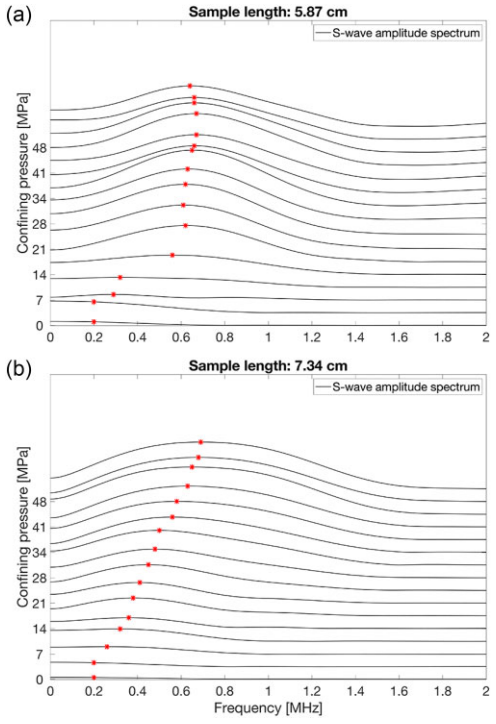

Figure B8. Amplitude spectra of extracted *S*-waveforms as a function of confining pressure. Amplitude spectra obtained by applying Fourier transform to the *S*-wave arrivals (Fig. B6) under dry conditions for sample lengths of (a) 5.87 cm and (b) 7.34 cm. Red circles indicate the peak frequency of the spectrum to highlight its pressure dependence.

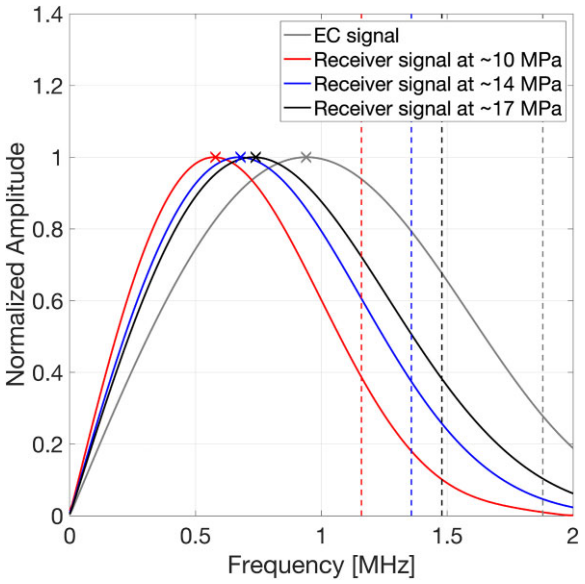

Figure B9. Signal spectra and frequency range used for the computation of the centroid frequency. The normalized amplitude spectrum of the EC signal represents the input spectrum, which exhibits a Gaussian-type shape. To compute the centroid frequency, we define the summation upper limit f_{up} in eq. (B2) imposing that f_s should be close to the frequency of the peak amplitude f_{max} for the EC signal. By defining $f_{\mathrm{up}} = kf_{\mathrm{max}}$, we find k to be around 1.82. The same factor is used for the spectra of the rock response (coloured curves) and results in a similar agreement between f_s and f_{max}.